



**Universität für Bodenkultur Wien**  
University of Natural Resources  
and Life Sciences, Vienna

# Master Thesis

## **Mechanistic studies on coproheme decarboxylase**

Submitted by

**Nina VALENTE, BSc**

in the framework of the Master programme

**Biotechnology**

in partial fulfilment of the requirements for the academic degree

**Diplom-Ingenieur**

Vienna, December 2021

Supervisor:

Priv.-Doz. DI Stefan Hofbauer, PhD  
Institute of Biochemistry  
Department of Chemistry

## Affidavit

I hereby declare that I have authored this master thesis independently, and that I have not used any assistance other than that which is permitted. The work contained herein is my own except where explicitly stated otherwise. All ideas taken in wording or in basic content from unpublished sources or from published literature are duly identified and cited, and the precise references included.

I further declare that this master thesis has not been submitted, in whole or in part, in the same or a similar form, to any other educational institution as part of the requirements for an academic degree.

I hereby confirm that I am familiar with the standards of Scientific Integrity and with the guidelines of Good Scientific Practice, and that this work fully complies with these standards and guidelines.

Vienna, December 2021

Nina VALENTE (*manu propria*)

*This thesis is dedicated to my wonderful grandmother Gerhild!*

*If you never ask, you will never know!!*

*Hanna Michlits, 2021*

## Acknowledgements

I would express my sincere gratitude to my principal supervisor Stefan Hofbauer for giving me the opportunity to conduct my master thesis in his working group. I am infinitely grateful for his scientific guidance, which I was allowed to experience during research and thesis preparation. I also want to thank him for his patience, understanding and enchanting character! You are highly appreciated!

Furthermore, I want to thank Hanna Michlits for her practical and technical advices she offered me during research and for her inspirational quote as an advice for future research.

I also would like to express my appreciation to the whole biochemistry-working group for the pleasant atmosphere I experienced during my stay. A big thank also goes to “The MASTERS”, Lina, Niki, Alex, Klara and Urban for many nice coffee breaks and lunch times together!

I am very appreciative of the emotional and motivational support I have experienced from my friends and colleagues all the way through my studies!!

My deepest thank and gratitude belong to my parents Gundis and Bruno and my brother Fabian for their endless love and support! I am unbelievably grateful to have you in my life!

Finally yet importantly, I want to thank Christof and our wonderful daughter Emma for the joy and happiness you bring to my life! I love you from the deepest of my heart! <3

## Abstract

With the elucidation of the coproporphyrin-dependent (CPD) heme biosynthesis pathway, the last of the three currently known heme biosynthesis pathways, and the discovery of the coproheme decarboxylase a new, potential inhibitory target for future antibiotics emerged. Coproheme decarboxylase catalyses the last step of the CPD-dependent pathway in which it drives the biphasic decarboxylation of coproheme into the final product heme *b*. The unique appearance of coproheme decarboxylase in the CPD-pathway, founds the potential as possible inhibitory target.

In this work, variants of corynebacterial coproheme decarboxylase (*CdChdC*) have been designed and established focusing on a selection of amino acid residues, which might be involved in the execution of the decarboxylation activity executed by *CdChdC*. The aim was to model a variant, which successfully terminates the reaction after the first decarboxylation cycle to produce the reaction intermediate monovinyl-monopropionyl- deuteroheme (MMD). The enzymes were then recombinantly expressed in *Escherichia coli* and characterized by means of biochemical and biophysical methods.

## Einleitung

Aktuell sind drei Haem-Biosynthesewege bekannt und mit der Entschlüsselung des Jüngsten, dem Coproporphyrin-abhängigen Biosyntheseweges, wurde auch die Coprohemedecarboxylase und ihr mögliches Potential als zukünftiger Angriffspunkt eines neuartigen Antibiotikums entdeckt. Die Coprohemedecarboxylase katalysiert den letzten Schritt des Coproporphyrin-abhängigen Biosyntheseweges und ist für die zweiphasige Decarboxylierung der Propionatseitenketten des Substrats Coproheme verantwortlich. Dieser enzymatische Schritt ist ein möglicher Angriffspunkt für die Entwicklung neuartiger Antibiotika, da in Coprohemedecarboxylasen nur in diesem Coproporphyrin-abhängigen Biosyntheseweg vorkommen.

Das Ziel dieser Arbeit war die Erschaffung von Varianten der corynebakteriellen Coprohemedecarboxylase, mit dem Fokus auf Aminosäuren, die eine Rolle in der Exekution des Reaktionsmechanismus spielen um eine Variante zu modellieren, die den Reaktionsmechanismus nach der ersten Decarboxylierung stoppt um das Reaktionsintermediat Monovinyl-Monopropionyl-Deuterohaem zu generieren. Die Enzymvarianten wurden anschließend rekombinant in *Escherichia coli* exprimiert und mit Hilfe biochemischer und biophysikalischer Methoden charakterisiert.

## Content

1	Introduction.....	10
1.1	<i>Corynebacterium diphtheriae</i> .....	10
1.1.1	Mode of action of the diphtheria toxin.....	10
1.2	Heme Biosynthesis pathways.....	11
1.2.1	The routes to 5-aminolevulinic acid (ALA) .....	12
1.2.2	Conversion of 5-aminolevulinic acid into uroporphyrinogen III.....	13
1.2.3	The protoporphyrin-dependent pathway .....	14
1.2.4	The siroheme pathway.....	15
1.2.5	The coproporphyrin-dependent pathway.....	16
1.3	Structure and function of coproheme decarboxylase (ChdC).....	17
1.3.1	Phylogenetic and structural classification.....	17
1.3.2	Cofactor orientation and substrate access channel.....	19
1.3.3	Active site of coproheme decarboxylase from <i>Corynebacterium diphtheriae</i> .....	19
1.3.4	Catalytic reaction mechanism .....	20
2	Aim of the thesis.....	23
3	Materials and Methods .....	25
3.1	Generation of CdChdC variants .....	25
3.1.1	Plasmid architecture.....	25
3.1.2	Primer designs .....	26
3.1.3	Site directed mutagenesis (SDM) .....	27
3.1.4	Heat-shock transformation of <i>E. coli</i> expression strain .....	28
3.1.5	Isolation of the SDM product .....	29
3.1.6	Determination of SDM product concentration .....	30
3.1.7	Verification of SDM product.....	30
3.1.8	Cryo cultures.....	30
3.2	Recombinant expression and purification of CdChdC variants.....	31
3.2.1	Test expression.....	31
3.2.2	Expression of CdChdC variants in Tuner (DE3) cells and cell harvest.....	31
3.2.3	Cell lysis .....	32
3.2.4	Metal chelate affinity chromatography .....	33
3.2.5	Quality control of protein purification .....	34
3.2.6	Concentration of eluate and determination of protein concentration.....	34
3.2.7	Size exclusion chromatography.....	34
3.3	Biochemical and biophysical characterization methods .....	35
3.3.1	Coproheme titration.....	35



3.3.2	Hydrogen peroxide titration followed by UV-vis spectroscopy .....	35
3.3.3	Chlorite titration followed by UV-vis spectroscopy .....	36
3.3.4	Steady-state kinetics .....	36
3.3.5	Pre-steady state kinetics .....	37
3.3.6	Electronic circular dichroism .....	38
3.3.7	MNP spin trapping.....	39
3.3.8	MALDI-TOF mass spectrometry.....	40
3.3.9	Size exclusion chromatography multiangle light scattering.....	40
4	Results .....	42
4.1	CdChdC variants.....	42
4.1.1	Tyrosine swap variants .....	42
4.1.2	Variants, investigating the role of threonine 172 .....	43
4.1.3	Variants, investigating the role of tyrosine 183 .....	44
4.2	Size exclusion chromatography multiangle light scattering.....	46
4.3	Coproheme titration.....	48
4.4	Hydrogen peroxide titration followed by UV-vis absorption spectroscopy.....	49
4.4.1	Tyrosine swap mutants .....	50
4.4.2	Variants, investigating the role of threonine 172 .....	51
4.4.3	Variants, investigating the role of tyrosine 183 .....	52
4.5	Chlorite titration followed by UV-vis absorption spectroscopy .....	54
4.5.1	Tyrosine swap mutants .....	54
4.5.2	Variants, investigating the role of tyrosine 183 .....	56
4.6	Pre-steady state kinetics .....	57
4.6.1	Tyrosine swap variants .....	58
4.7	Steady-state kinetics .....	61
4.8	Electronic circular dichroism .....	63
4.8.1	Far UV electronic circular dichroism (ECD).....	63
4.8.2	Thermostability .....	64
4.9	MNP spin trapping.....	67
4.10	Matrix assisted laser desorption/ionization.....	68
4.10.1	Tyrosine swap variants .....	69
4.10.2	Variants, investigating the role of tyrosine 183 .....	70
5	Discussion .....	72
6	Conclusion .....	78
7	References.....	79

# 1 Introduction

## 1.1 *Corynebacterium diphtheriae*

*Corynebacterium diphtheriae*, formerly known as Klebs-Löffler bacterium, belongs to the family of Corynebacteriaceae, which comprises more than 100 members (1). *C. diphtheriae* is a Gram-positive, non-motile, aerobic and rod-shaped bacterium, with a characteristic, club-shaped morphology. Their specific club-shape can be attributed to the presence of metachromatic granules on one or both sides of the bacterium (2). *C. diphtheriae* occur as toxigenic and non-toxigenic strains and they are classified into four biovars, namely *gravis*, *mitis*, *intermedius* and *belfanti* (3), according to their biochemical and physiological properties. *C. diphtheriae* can cause an acute infection of the mucosal membrane of the upper respiratory tract as well as ulcerating skin lesions (2). *C. diphtheriae* is transmitted by droplets or nasopharyngeal secretions (4). Cells of the nasopharyngeal region are susceptible for infections caused by *C. diphtheria* and unbridled proliferation results in the occurrence of a white, leather-like pseudomembrane (5). The pseudomembrane consists out of cells from *C. diphtheriae* and lysed host cell, which have been affected by the secretion of the diphtheria toxin.

### 1.1.1 Mode of action of the diphtheria toxin

The diphtheria toxin (DT) is a protein toxin composed of 535 amino acids and a molecular weight of 58.348 kDa. Structural studies in 1992 revealed a Y-shaped quaternary structure (6), holding three discrete folding domains (7). Each domain is named according to their respective function: the C domain is responsible for the execution of the catalysis of the DT; the T domain drives the translocation of the toxin and the R domain enables the binding of the toxin to the host cell receptor (7). A trypsin sensitive is located between the T and C domain, which enables the cleavage of the protein into fragment A and B upon infection of the host cell.

As an initial step of host cell intoxication, the DT acquires access into the host cell via receptor-mediated endocytosis, which is promoted by the R domain of the toxin. The acidic conditions within the endosome induce a conformational change of the DT. The mechanism of this conformational change is still elusive (6) but it promotes the ability to the T domain of the DT to insert into the lipid bilayer of the endosome. The insertion of the T domain into the

endosomal bilayer results in the formation of an ion channel through which the DT escapes the endosome to the cytosol. To be able to passage the lipid bilayer, partial unfolding of the C domain is required (7). In the cytosol, cytosolic host chaperones mediate the rearrangement of the DT, followed by the release of fragment A, carrying the C domain of the toxin. The catalytic domain drives the transfer of ADP-ribose from NAD to elongation factor 2 to block the cellular protein biosynthesis.

## 1.2 Heme Biosynthesis pathways

Heme is one of the most meaningful molecules in nature and it is a modified tetrapyrrole. The class of modified tetrapyrroles is regarded as pigments of life (9) as they play essential roles in many biological functions. Besides heme, chlorophyll, corrin, siroheme, heme *d* and coenzyme F<sub>430</sub> are representatives of modified tetrapyrroles. All representatives derive from the common progenitor, uroporphyrinogen III, via divergent biosynthetic pathways. Modified tetrapyrroles share a common macrocyclic porphyrin structure composed of four pyrrole rings linked by methine bridges. The letters A to D specify the pyrrole rings in a clockwise manner. The basic macrocyclic structure enables the coordination of diverse metal atoms. The nature of the chelated metal atom in modified tetrapyrroles is as diverse as the nature of their peripheral side chains associated to the porphyrin ring. This diversity is reflected by the broad range of functions, in which modified tetrapyrroles are involved in.

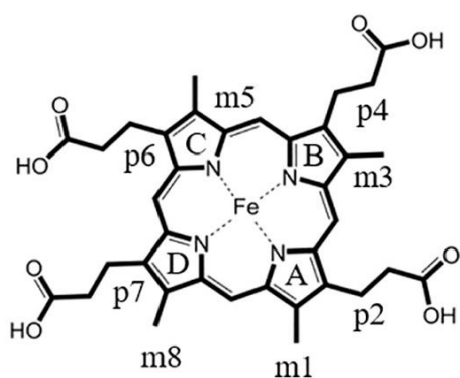


**Figure 1 :Chemical structure of heme *b*** (Hofbauer et al (2021). *Understanding molecular enzymology of porphyrin-binding  $\alpha + \beta$  barrel proteins - One fold, multiple functions.*)

Heme *b*, is the most abundant of all modified tetrapyrroles, being involved in gas sensing and transport, electron transport, catalysis, signalling (10; 9) and it is present as prosthetic group in many hemoproteins. Moreover, heme *b* plays an eminent role in the pathogenesis of some bacteria.

Heme *b* carries an iron as central metal atom, which can be present in different oxidation states.

The iron is coordinated by four nitrogen atoms of the protoporphyrin and by one nitrogen contributed from a histidine in the active site. Heme

*b* holds two vinyl groups attached to pyrrole rings A and B and two propionyl groups on rings C and D.

The cellular heme *b* homeostasis is ensured by complex heme uptake systems and the *de novo* heme synthesis, which can be pursued via three different heme biosynthesis pathways, namely the protoporphyrin-dependent pathway (PPD-pathway), the siroheme-dependent pathway and the coproporphyrin-dependent pathway (CPD-pathway). Heme biosynthesis appears in three phases: (I) the synthesis of 5-aminolevulinic acid (ALA), (II) the conversion of ALA into uroporphyrinogen, which constitutes a common origin for (III) the transformation of uroporphyrinogen into heme *b* via three biosynthesis routes.

### 1.2.1 The routes to 5-aminolevulinic acid (ALA)

The non-proteinogenic amino acid 5-aminolevulinic acid, is uniquely used as C5 intermediate and precursor in the heme biosynthesis pathway. 5-aminolevulinic acid, exclusively provides the carbon and nitrogen atoms needed for heme biosynthesis (12). Two routes are offered to the precursor ALA; the C4 or shemin pathway and the C5 pathway. Eukaryotes, fungi and non-sulfur bacteria utilize the C4 pathway whereas higher plants, archaea and bacteria take advantage of the C5 pathway.

The key enzyme of the C4 pathway is the homodimer ALA synthase. ALA synthases (AlaS) catalyse the condensation reaction of succinyl CoA and glycine to yield ALA. The reaction is dependent on the cofactor pyridoxal phosphate (PLP), the active form of vitamin B6. PLP is bound to AlaS, acting as electrophilic catalyst. Glycine attaches to the PLP to form a Schiff base. A Proton abstracts and succinyl CoA binds to the glycine forming the intermediate 2-amino-3-ketoadipate. Subsequently the CoA moiety and carbon dioxide are released resulting in 5-aminolevulinic acid (9).

The emergence of the C5 pathway is glutamate, more precisely, glutamyl-tRNA. Glutamyl-tRNA associates with glutamyl-tRNA-reductase (GtrR), an asymmetric V-shaped enzyme. GtrR holds a catalytic, nucleotide-binding fold- and a dimerization domain arranged along a spinal helix (13). Upon binding of glutamyl-tRNA a conformational change is induced to oppose the catalytic and the nucleotide-binding fold, carrying the cofactor NADPH. A catalytic cysteine residue in the active site promotes the release of the tRNA and the formation of an enzyme

bound thioester. Moreover, a hydride from the co-factor NADH is transferred to yield the intermediate glutamate semialdehyde. The glutamate semialdehyde aminomutase (GsaM), an enzyme closely related to AlaS, binds to the glutamate semialdehyde-enzyme complex to prevent degradation of the intermediate. GsaM holds pyridoxamine-5-phosphate as co-factor to which the GSA binds to form 5-diaminovalerate. 5-diaminovalerate undergoes a rearrangement process in which the amino group is transferred to the C5 to yield 5-aminolevulinic acid.

### 1.2.2 Conversion of 5-aminolevulinic acid into uroporphyrinogen III

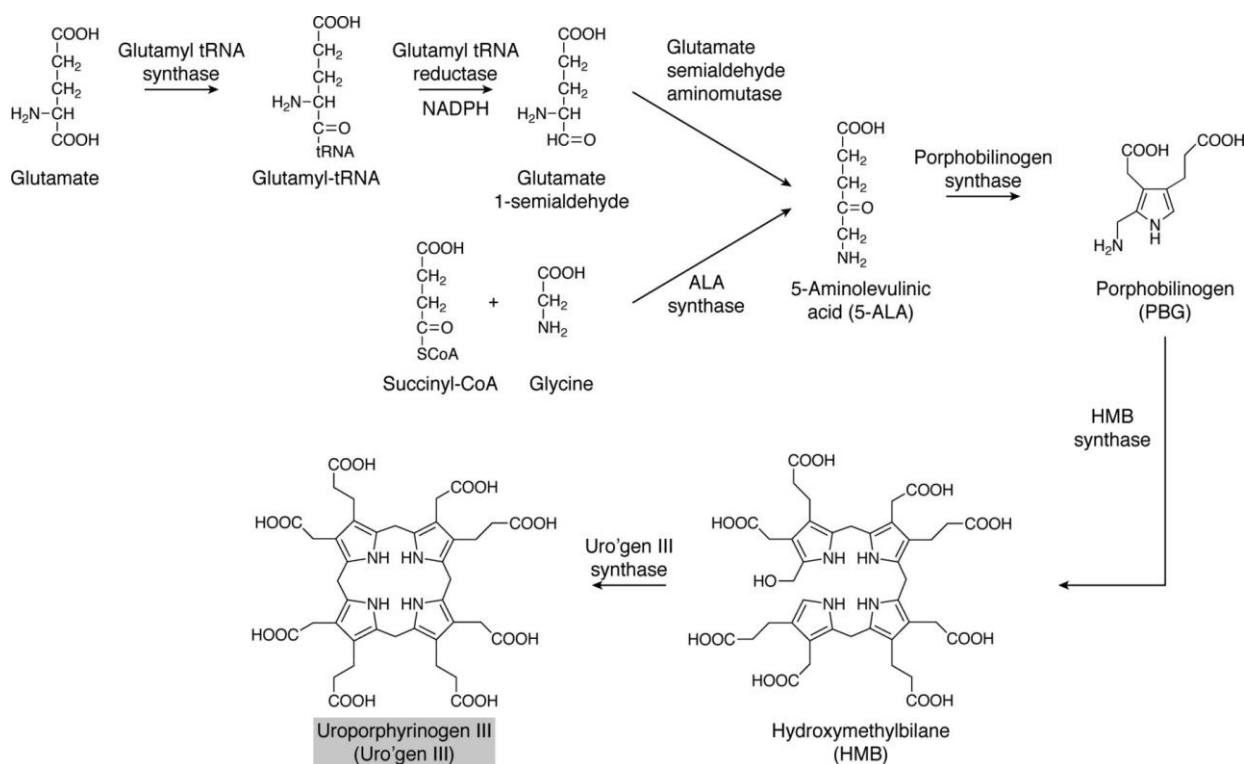


Figure 2 (Bryant, D. A., et al; (2020). Biosynthesis of the modified tetrapyrroles—the pigments of life.) The routes to ALA can lead via the C4 (Shemin) or the C5 pathway. The C4 pathway guides to ALA through the condensation of Succinyl-CoA and glycine, mediated by the ALA synthase. The C5 pathway commences with the association of glutamyl-tRNA with glutamyl-tRNA reductase which drives the conversion of glutamyl-tRNA into glutamate 1-semialdehyde(GSA). GSA drives the rearrangement process of the amino group to yield ALA. Two ALA molecules are consequently condensed to porphobilinogen(PBG) by porphobilinogen synthase. Hydroxymethylbilane synthase combines four PBG molecule yielding hydroxymethylbilane(HMB). HMB is then converted into uroporphyrinogen by uroporphyrinogen III synthase.

The conversion of 5-aminolevulinic acid into uroporphyrinogen III (URO) is a conserved process executed in three enzymatic reactions. The mechanism is identical in all tetrapyrrole-

synthesising organism. To yield one molecule of URO eight molecules of ALA are required. First, porphobilinogen synthase is responsible for the asymmetric condensation of two ALA molecules yielding porphobilinogen. Hydroxymethylbilane synthase combines four porphobilinogen molecules from head to tail (8) to the linear tetrapyrrole precursor hydroxymethylbilane under release of ammonium. Uroporphyrinogen III synthase modifies the pyrrole ring D to enable cyclization of the macrocyclic structure of the tetrapyrrole (14; 15).

### 1.2.3 The protoporphyrin-dependent pathway

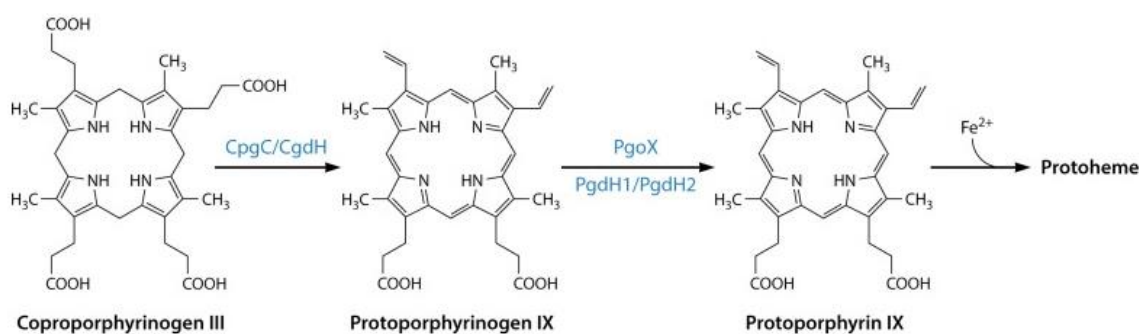


Figure 3: (Dailey et al., 2017, *Prokaryotic Heme Biosynthesis: Multiple Pathways to a Common Essential Product*) The conversion of coproporphyrinogen III is driven by coproporphyrinogen oxidase which mediates the decarboxylation of propionates at side chains A and B. The yielded protoporphyrinogen is then effected by a six electron loss and the introduction of three double bonds, both mediated by protoporphyrinogen oxidase. As ultimate step, the ferrous iron is inserted by protoporphyrin IX-ferrochelatase yielding heme b.

For a long time, the protoporphyrin-dependent or “classic” heme biosynthesis pathway was believed to be the only route for heme synthesis. This route to heme *b* commences with the decarboxylation of four carboxyl groups from the carboxymethyl side chains of URO. Uroporphyrinogen decarboxylase utilizes the electrons of the pyrrole macrocycle to perform the reaction. Decarboxylation starts at the D ring and progresses in a clockwise manner to ring A. Coproporphyrinogen III is the product of this initial step. For the second phase of the PPD pathway, coproporphyrinogen III attaches to the active site of coproporphyrinogen oxidase, which converts the propionate side chains A and B into vinyl groups under release of two water molecules and two carboxyl groups. The substrate stays bound to the active site for both decarboxylation reactions (16). The yielded, fully reduced protoporphyrinogen IX, is fully oxidized by PPO (protoporphyrinogen oxidase). PPO catalyzes the removal of six electrons

and protons resulting in the introduction of three double bonds (9). The product of this oxidation is protoporphyrin IX into which protoporphyrin IX-ferrochelatase inserts ferrous iron, in a not yet completely elucidated mechanism (16), as an ultimate step of the classical heme biosynthesis pathway.

#### 1.2.4 The siroheme pathway

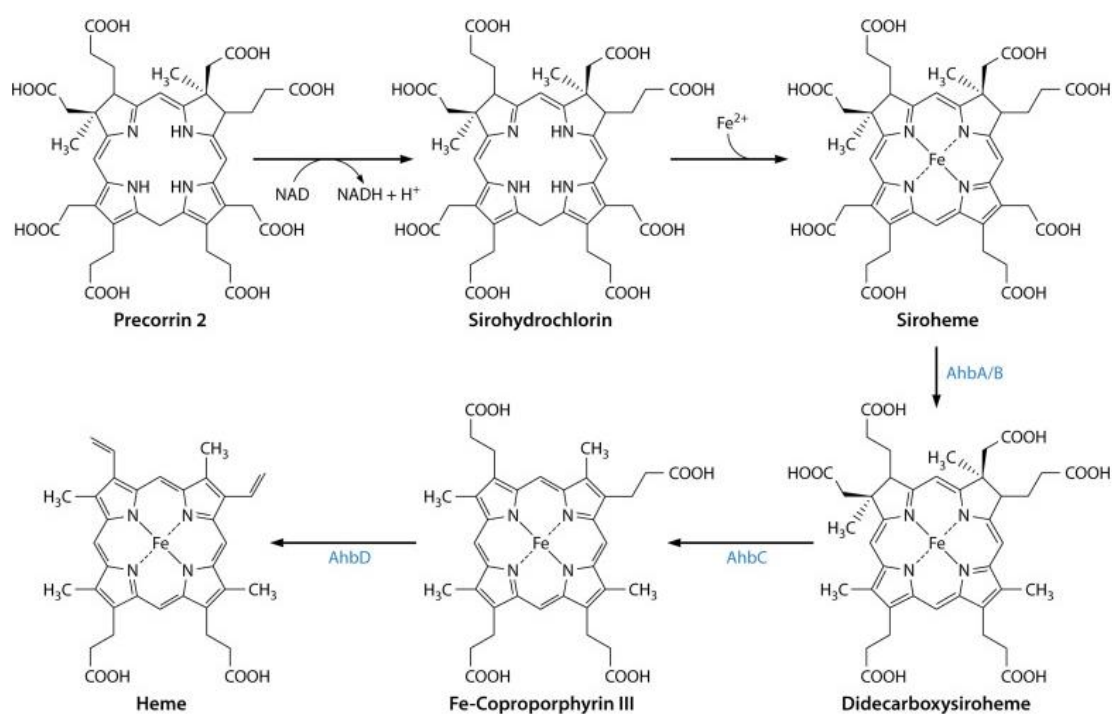


Figure 4: (Dailey et al., 2017, *Prokaryotic Heme Biosynthesis: Multiple Pathways to a Common Essential Product*): The siroheme pathway initiates with the conversion of URO into precorrin 2. An NAD<sup>+</sup>-dependent dehydrogenase drives the abstraction of two protons and two electrons resulting in the formation of two double bonds and the intermediate sidrohydrochlorin. Sidrohydrochlorin is converted into siroheme through the insertion of ferrous iron. The acetic side chains of siroheme are decarboxylated by siroheme-decarboxylase yielding coproporphyrinogen III. Finally, the carboxymethyl side chains are decarboxylated yielding heme b.

The siroheme pathway or alternative pathway was the first non-canonical heme biosynthesis pathway described. Sulfate-reducing bacteria and some archaea synthesize heme via the siroheme pathway.

For the siroheme route of heme, the C2 and C7 of the URO macrocycle is methylated by uroporphyrinogen III methyltransferase, which requires S-adenosyl methionine (SAM) as cofactor resulting in the intermediate precorrin-2. Two electrons and two protons are then abstracted from the precorrin-2 molecule by an NAD<sup>+</sup>-dependent dehydrogenase to establish

an additional double bond forming sidrohydrochlorin. Sidrohydorchlorin is then converted into siroheme by the insertion of ferrous iron, which is mediated through chelatase activity. During the chelating process two protons are removed from the nitrogens of the pyrrole rings (9). Next, siroheme undergoes decarboxylation of its acetic acid side chains attached to ring C and D. The decarboxylation reaction is mediated by siroheme-decarboxylase, a dimeric enzyme, composed out of subunits AhbA and AhbB. In the next phase, the carboxymethyl side chains of rings A and B are decarboxylated by AhbC, a radical SAM decarboxylase, resulting in Fe-coproporphyrin III. As ultimate step of the siroheme-dependent heme biosynthesis pathway, the propionate groups are converted into vinyl groups by AhbD, yielding heme *b* (9).

### 1.2.5 The coproporphyrin-dependent pathway

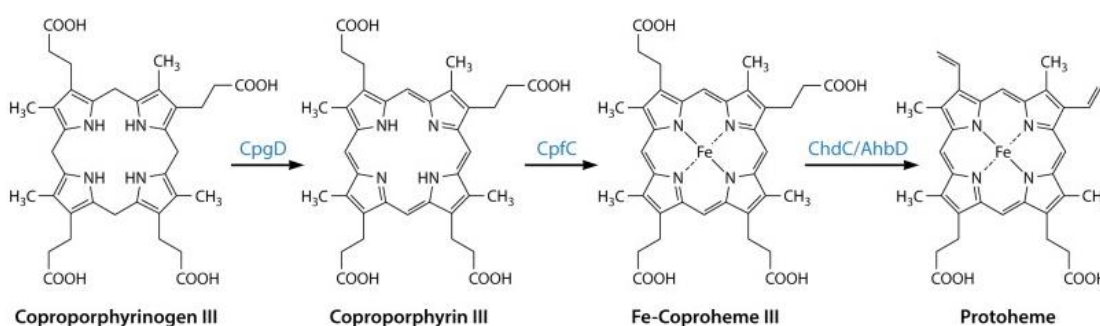


Figure 5: (Dailey et al., 2017, *Prokaryotic Heme Biosynthesis: Multiple Pathways to a Common Essential Product*): The coproporphyrin dependent pathway commences with the decarboxylation of URO by uroporphyrinogen decarboxylase yielding coproporphyrinogen III. coproporphyrinogen oxidase mediated the removal of six electrons and drives the conversion into coproporphyrin III. Through the distortion of the tetrapyrrole macrocycle, ferrous iron can be inserted by coproporphyrin ferrochelatase. Ultimately, coproheme decarboxylase mediates the decarboxylation of the propionate side chains into vinyl groups yielding heme *b*.

The coproporphyrin-dependent (CPD) heme biosynthesis pathway is the most recently described pathway. It was only elucidated some time ago and was first described in 2015 (18). Mainly Gram-positive bacteria utilize this route to generate heme *b*, but also some Gram-negative (diderm) and intermediate bacteria (23).

The CPD pathway shares the initial step with the classic (PPD) pathway, in which URO is decarboxylated by UroD to yield coproporphyrinogen III. After the generation of coproporphyrinogen III, the route branches towards coproporphyrin III as the next intermediate instead of protoporphyrinogen IX. CpoX (coproporphyrinogen oxidase) mediates



the loss of six electrons and protons and drives the conversion of coproporphyrinogen III into coproporphyrin III. This reaction follows the same principle and mechanism as the conversion of protoporphyrinogen into protoporphyrin IX in the classical pathway (9). Consequently, iron is inserted into coproporphyrin III mediated by the chelatase activity of coproporphyrin ferrochelatase (CpfC). The iron insertion is enabled by the distortion of the tetrapyrrole macrocycle (19) yielding coproheme. As ultimate step of the coproporphyrin-dependent biosynthesis pathway, coproheme decarboxylase (ChdC) catalyzes the decarboxylation of the propionate side chains of coproheme, requiring hydrogen peroxide as co-substrate.

### 1.3 Structure and function of coproheme decarboxylase (ChdC)

#### 1.3.1 Phylogenetic and structural classification

Coproheme decarboxylases (ChdC), formerly known as HemQ, have been classified as members of the peroxidase-chlorite dismutase superfamily, and phylogenetic analysis revealed a unique, conserved structural sequence motif (-Y-P-M/F-X-K/R) (23).

By now four phylogenetic clades of ChdCs have been identified, each sharing a conserved, essential tyrosine. The tyrosine orients towards the propionate on position 2 of the coproheme and is of utmost importance as it is the catalytic radical site and consequently responsible for the execution of the decarboxylation reaction driven by ChdC (27). In the proximity of the propionate 4, a positively charged residue, either lysine or arginine is found, which is essential for the smooth operation of the catalytic turnover and the coordination of p4. A methionine or a phenylalanine, positioned between the propionates 2 and 4, is assigned as a benefactor on the stability of the active site.

Although this conserved structural motif has been revealed, each distinct clade shows their peculiar characteristics. Clade 1 ChdCs comprise representatives of the phylum Firmicutes to which *Staphylococcus aureus* and *Listeria monocytogenes* belong to. Most structural, mechanistic and kinetic data have been obtained through examination of firmicute ChdC. Actinobacterial ChdC, with which *Corynebacterium diphtheriae* are associated, are phylogenetically categorized into clade 2.

The comparison of actinobacterial and firmicute ChdC reveal obvious divergences. A glance at the distal site of the active site in Actinobacteria discloses a histidine on position 118 (*CdChdC* numbering), acting as a distal base to heterolytically cleave the substrate hydrogen peroxide. The histidine is located on the flexible linker loop with a distance of 5Å from the coproheme iron (24). This optimal distance between the coproheme iron and the histidine is owed to the orientation of the linker loop, which points towards the active site. In firmicute ChdC a distal base has not yet been identified. The presence of the deprotonating histidine in Actinobacteria promotes the ability to more efficiently convert coproheme into heme *b*.

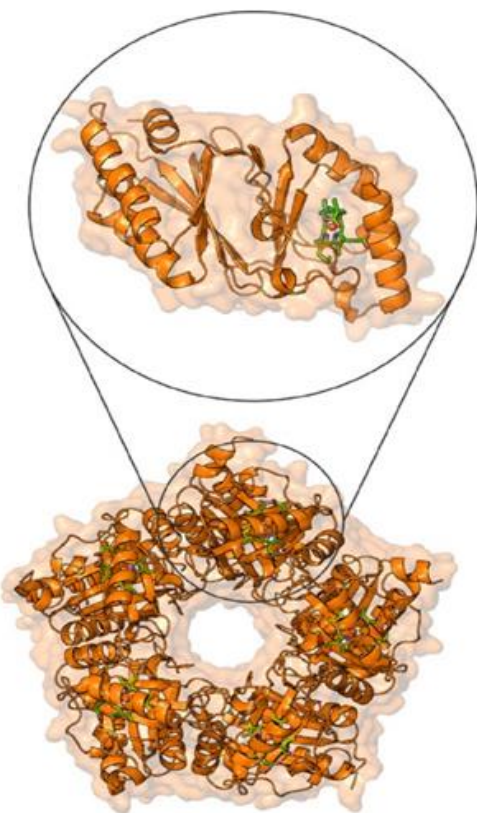


**Figure 6: Overall structure of coproheme decarboxylase** (Michlits, et al. (2020). *Actinobacterial Coproheme Decarboxylases Use Histidine as a Distal Base to Promote Compound I Formation.*). ChdC crystal structure representing the homopentameric quaternary structure of actinobacterial ChdC as well as the structural architecture of one ChdC subunit.

Beside this characteristic histidine, the distal side of actinobacterial ChdC holds an alanine on position 170, unique for representatives of this clade. The distal side of firmicute ChdC displays a glutamine, possibly acting as a six coordinated low-spin (6cLS) ligand. Due to this coordinating ability, a regulating function can be attributed to the glutamine (29).

In both phyla, structural studies bared the absence of a conserved hydrogen bond partner (29) to the iron-coordinating histidine on the proximal side of the active site. At the respective position, actinobacterial and firmicute representative differ in the binding partner with the propionate p4. In Actinobacteria, an arginine coordinates the p4 whereas this function is executed by a lysine in firmicute ChdCs.

Revised phylogenetic analysis classify coproheme decarboxylases into the dimeric  $\alpha+\beta$  barrel structural superfamily (29). The members of this structural superfamily share a ferredoxin-like fold as the common tertiary structural element, offering a broad functional variety to its representatives. One subunit of the dimeric  $\alpha+\beta$  barrel superfamily has a size of 250-300 amino acids and consists out of two ferredoxin-like folds. One ferredoxin-fold composes two terminal  $\beta$ -strands, which connect with two central  $\beta$ -

strands via a hydrogen bond network, forming an antiparallel  $\beta$ -sheet. Two  $\alpha$ -helices flank the antiparallel  $\beta$ -sheet on one side, arranging a long symmetrical hairpin structure. The N-terminal ferredoxin fold connects with the C-terminal ferredoxin fold via a linker loop, with a size of approximately 20-30 amino acids. The C-terminal ferredoxin-like fold offers a binding cleft into which the redox active substrate, coproheme, can bind. ChdC assembles as a homopentameric (26) protein.

### 1.3.2 Cofactor orientation and substrate access channel

Coproheme decarboxylase utilizes Fe-coproporphyrin III (coproheme) as a redox co-factor. Coproheme is an iron containing porphyrin, in which the iron is coordinated as central atom by four pyrrole rings. One propionate group bound to each pyrrole ring characterizes coproheme. In the active site, four nitrogen atoms of the pyrrole rings and one nitrogen atom from the proximal histidine contribute in the coordination of the coproheme, leaving one coordination site of the iron vacant.

The prosthetic group arranges into the binding cleft of the C-terminal ferredoxin-fold with the propionates p6 and p7 directed towards the solvent and an orientation rotated by 90° compared to the respective positions in heme *b*. Coproheme binding occurs in two subsequent steps: initially the coproheme binds through coordination of the central iron by a histidine. The binding process induces a structural rearrangement and the generation of non-covalent interactions between the co-factor and the protein (29; 30).

The co-factor and the substrate penetrate into the active site via a substrate access channel mainly defined by the linker loop. The calculated bottleneck radius of the highly flexible substrate access channel range between 1-2.5 Å (29) The location of the substrate access channel enables a lateral entry to the active site of the enzyme.

### 1.3.3 Active site of coproheme decarboxylase from *Corynebacterium diphtheriae*

The active site is the core element of an enzyme, where it executes its function. The active site of a heme containing enzyme holds two sides: the proximal and the distal side of the heme. On the proximal side the iron center of coproheme is coordinated by the nitrogen of the

histidine. Furthermore, an extensive H-bond network harbours the prosthetic group to the active site. The propionate p2 is stabilized by two hydrogen bonds, which interact with the arginine on position 208 and the threonine on position 205 via a water molecule.

The propionate on position 4 (p4) forms non-covalent bonds with a tryptophan on position 143. The distal site of the active site of ChdC discloses a high level of diversity within their phylogenetic clades. The catalytic tyrosine on position 135, a histidine on position 118 and an alanine on position 207 characterize the distal site of actinobacterial ChdC. The histidine is situated on the flexible linker loop near the substrate entry locus, where it executes its function as a distal base to deprotonate the incoming substrate, which most probably is hydrogen peroxide. The alanine on position 207 is highly conserved in actinobacteria (23). On the distal side, the coproheme is bound to the active site by the establishment of hydrogen bond between the propionate at position 6 (p6) and the asparagine on position 115. Beside its function as distal base, the histidine on position 118 is also involved in a hydrogen bond with the propionate p7 (24).

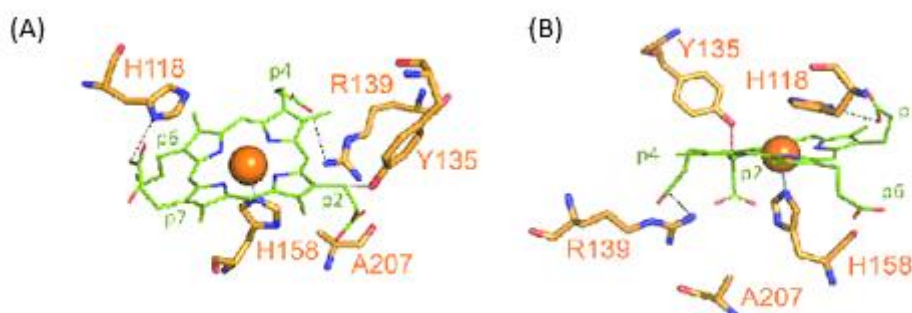


**Figure 7 : Active site of CdChdC:** (Sebastiani, F. et al.; (2021). Reaction intermediate rotation during the decarboxylation of coproheme to heme *b* in *C. diphtheriae*) (A) Distal side of the active site of coproheme-bound ChdC from *C. diphtheriae*. (B) Overview on crucial amino acid residues within the active site of coproheme-bound-ChdC from *C. diphtheriae*.

#### 1.3.4 Catalytic reaction mechanism

Coproheme decarboxylase catalyzes the last step of the coproporphyrin-dependent heme biosynthesis pathway. ChdC converts the substrate coproheme into heme *b* in a biphasic reaction. For the initiation of the reaction, the natural substrate hydrogen peroxide is required, acting as a two-electron donor. *In vitro* peroxyacetic acid, flavin mononucleotide and sodium chlorite were identified as alternative substrates to launch the reaction (27; 29). For

the complete conversion of coproheme into heme *b*, a 2:1 stoichiometry of hydrogen peroxide and coproheme is required (24).

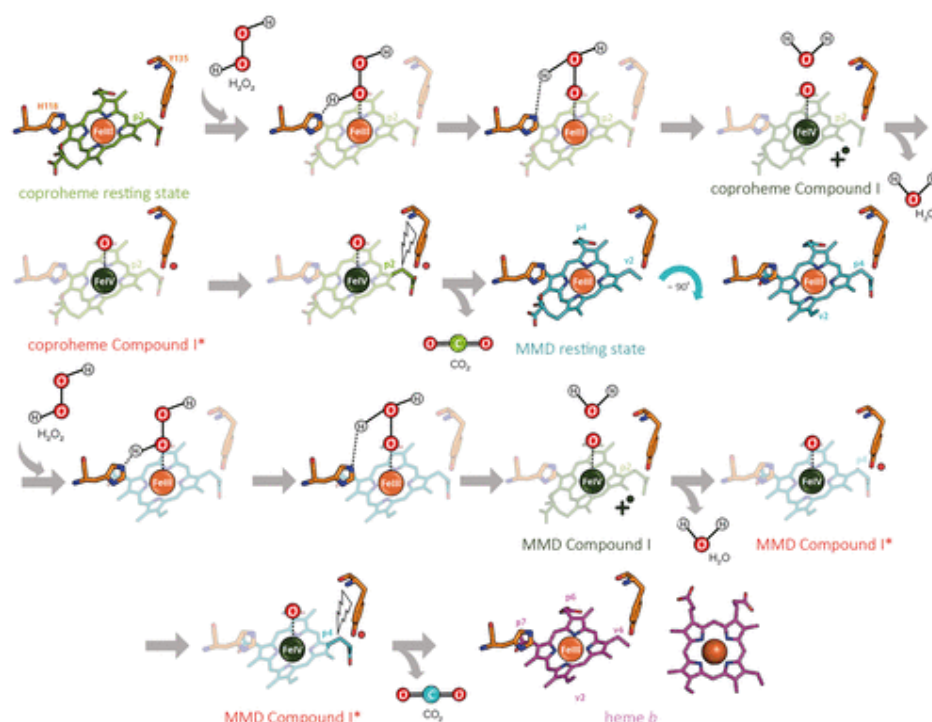
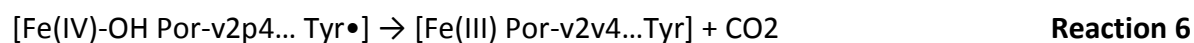
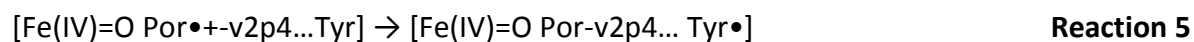
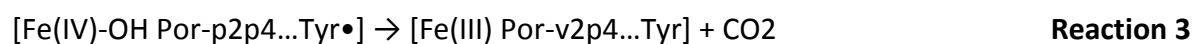
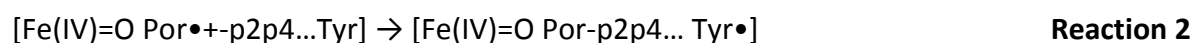
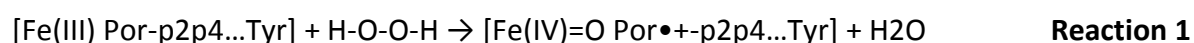


**Figure 8: Reaction mechanism of CdChdC** (Michlits, H. et al.; (2020). Actinobacterial Coproheme Decarboxylases Use Histidine as a Distal Base to Promote Compound I Formation): Elucidated reaction mechanism of coproheme decarboxylase. The incoming substrate hydrogen peroxide acting as two electron donor to oxidize the ferric resting state of the coproheme for compound I formation. An internal electron transfer promotes compound I\* formation and the radicalisation of the tyrosine 135. The radicalisation promotes the ability to perform the attack of the  $\beta$  carbon atom of the propionate at position p2. The intermediate MMD is formed. The MMD is affected by an reorientation by  $90^\circ$  to move the p4 to the proximity of the tyrosine 135. After this rearrangement a second decarboxylation takes place in the same manner as the first one.

In the presence of hydrogen peroxide, as sparking oxidant, two electrons are donated to oxidize the ferric resting state of the coproheme to promote compound I formation (**Reaction 1**). Histidine 118 deprotonates the incoming hydrogen peroxide through heterolytic cleavage. The presence of this distal base accelerates Compound I formation compared to firmicute ChdC representatives (25). An internal electron transfer promotes the formation of the catalytically active Compound I\* [Fe(IV)=O Por-p2p4... Tyr\*] (**Reaction 2**), which includes the conversion of the tyrosine 135 into a neutral radical species. This conversion promotes the ability to perform a nucleophilic attack on the  $\beta$  carbon of the propionate at position p2. With this decarboxylation reaction, the propionate on position p2 is converted into a vinyl group upon release of carbon dioxide, forming the reaction intermediate monovinyl-monopropionyl deuteroheme (MMD) [Fe(IV) Por-v2p4... Tyr] (**Reaction 3**). After the completion of this first decarboxylation step, the intermediate undergoes a  $90^\circ$  rotation (25) to bring the propionate p4 to the proximity of the catalytic tyrosine. This reorientation process

was revealed by X-ray crystallographic analysis and ruled out speculations on a long-range internal electron transfer and the presence of two active sites (31; 23). After reorientation, a second reaction cycle is initiated by hydrogen peroxide. This time, the ferric resting state of the coproheme is oxidised to promote compound I formation [Fe(IV)=O Por•+-v2p4...Tyr ] (**Reaction 4**) , including another radicalisation of the tyrosine [Fe(IV)=O Por-v2p4... Tyr•] (**Reaction 5**). The tyrosine then attacks the β-carbon atom of the propionate at position p4, which is converted into a vinyl group under the release of carbon dioxide to yield the heme *b* protein. [Fe(III) Por-v2v4...Tyr] (**Reaction 6**). The generated heme *b* is ready to be distributed within the cell.



## 2 Aim of the thesis

With the discovery of the coproporphyrin-dependent heme biosynthesis pathway in 2015, a novel target for potential antibiotic therapies emerged. Coproheme decarboxylase (ChdC), which catalyse the terminal step in this heme biosynthesis pathway, was identified to be a promising candidate. Until then, there is still a need for research on the reaction mechanism of coproheme decarboxylase. The aim of this thesis was to specifically interfere and manipulate the reaction mechanism of ChdC to terminate the enzymatic reaction after the formation of the 3-propionate intermediate, monovinyl-monopropionyl deuteroheme (MMD).

In the first part of this thesis, a tyrosine-swap was implemented. Therefore, the reactive and catalytically essential tyrosine, located in the proximity of the propionate at position 2, was relocated to the vicinity of the propionate at position 4. Tyrosine 135 was substituted with an alanine or tryptophan and a new tyrosine was inserted at position 183, replacing a tryptophan. These mutations are supposed to stimulate MMD formation. Furthermore, the impact of two reactive tyrosines was investigated in the single mutant, in which tryptophan 183 was replaced by tyrosine, here the native tyrosine at position 135 is still present.

As a second step, the influence of the incorporation of a reactive tyrosine into a solely MMD producing variant of *CdChdC* was examined. For this purpose, the *CdChdC* variant H118F was equipped with a tyrosine on position 183 to investigate its potential decarboxylation ability. The reorientation of the MMD in the H118F variant is sterically blocked by the exchange of the histidine 118 by a phenylalanine. With a tyrosine in the proximity of the propionate on position 4, the potential ability to produce heme *b* was probed.

Furthermore, it was supposed that the removal of the threonine at position 172 would facilitate and direct the electron transfer towards the tyrosine on position 183 to stimulate the formation of MMD. The exchange of the threonine 172 by an alanine is accompanied by a difference in polarity, which diverts electrons towards the propionate on position 4. The difference in size of threonine and alanine depletes the passage towards the propionate at position 4.

Besides the generation of an MMD producing *CdChdC* variant, this thesis focuses on the biochemical and biophysical characterization of *CdChdC* variants, including spectroscopic analysis, kinetic investigations and observation of thermal stability characteristics.



### 3 Materials and Methods

#### 3.1 Generation of *CdChdC* variants

##### 3.1.1 Plasmid architecture

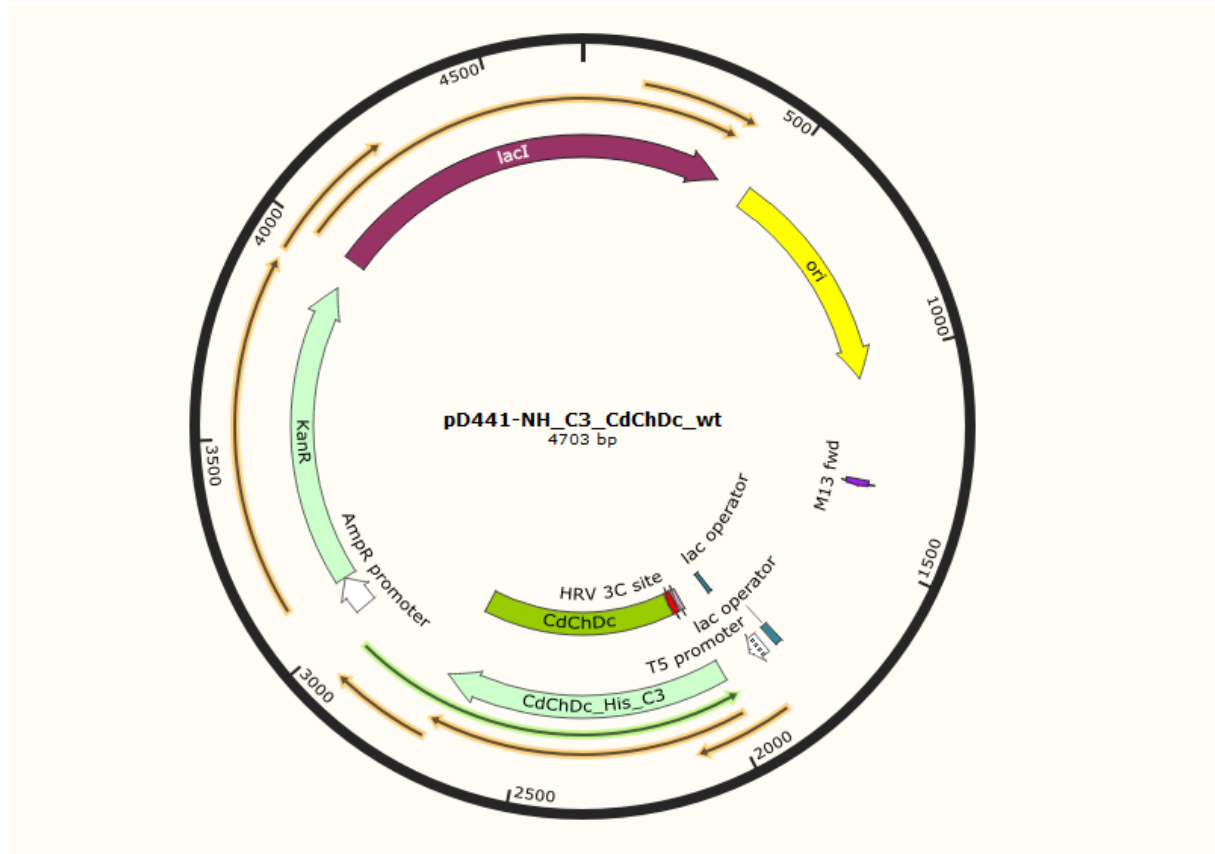


Figure 9: pD441\_NH vector plasmid containing the gene of interest with a poly His-Tag and a HRV Precision protease cleavage site under control of a lac promoter. A kanamycin resistance gene is present as a selection marker.

The wild-type *CdChdC* and its variants were recombinantly expressed in an *E. coli* Tuner (DE3) expression system. The gene coding for *CdChdC* was inserted into a pD441\_NH vector plasmid. The vector has a length of 4703 bp and carries the *CdChdC* gene, which is under the control of the lac promoter. The lac promoter is required to induce gene overexpression upon addition of IPTG, the structural analog of allolactose. Furthermore, as a selection marker, a Kanamycin resistance gene is present in the PD441\_NH vector. The *CdChdC* gene was also provided with a poly His-Tag to enable protein purification by His trap purification. In connection to the poly His Tag an HRV 3C cleavage site is found within the pD441\_NH, to which

an HRV Precision protease can bind to release the purified protein from the His trap column and to remove the poly His Tag to obtain the recombinant protein in its native state.

### 3.1.2 Primer designs

Primers for the introduction of distinct point mutations were designed with the help of the Quick-change Lightning Primer design tool provided by Agilent technologies. By the exchange of single amino acid residues their influence on the reaction mechanism can be investigated. Therefore, the template DNA was uploaded to the design tool and translated into its amino acid sequence. Then the desired amino acid was selected and the replacement character of choice was chosen, to finally obtain a suitable primer sequence and its corresponding melting temperature. The primer was then ordered and purchased at Microsynth.

The following primers for their corresponding variants have been designed:

**Table 1:** List of primers used for the generation of CdChdC variants.

Primers for site directed mutagenesis			
Designation	Sequence	Orientation	Variant
CdChdC_H118F	gctgagttcaaccgcagctttctgccgtcgttcattat	fw	H118F
CdChdC_H118F	ataatgaacgacggcagaaagctgcggttgaactcagc	rev	
CdChdC_H118F	gctgagttcaaccgcagctttctgccgtcgttcattat	fw	H118FW183Y
CdChdC_H118F	ataatgaacgacggcagaaagctgcggttgaactcagc	rev	
CdChdC_W183Y	gcctcaaaccgagcatatactcataatcacccagtgc	rev	
CdChdC_W183Y	gcactgggtgattatgagtatatgctggcggttgaggc	fw	
CdChdC_H118F	gctgagttcaaccgcagctttctgccgtcgttcattat	fw	H118FY135AW183Y
CdChdC_H118F	ataatgaacgacggcagaaagctgcggttgaactcagc	rev	
CdChdC_W183Y	gcctcaaaccgagcatatactcataatcacccagtgc	rev	
ChdChdC_W183Y	gcactgggtgattatgagtatatgctggcggttgaggc	fw	
CdChdC_Y135A	gcgcacgaacggtgcaaccgtaatccaatcacccggg	fw	
CdChdC_Y135A	cccgggcgattggattacggttgaccgttcgtgcgc	rev	
CdChdC_W183Y	gcctcaaaccgagcatatactcataatcacccagtgc	rev	W183Y
CdChdC_W183Y	gcactgggtgattatgagtatatgctggcggttgaggc	fw	
CdChdC_W183Y	gcctcaaaccgagcatatactcataatcacccagtgc	rev	W183YY135A
CdChdC_W183Y	gcactgggtgattatgagtatatgctggcggttgaggc	fw	
CdChdC_Y135A	gcgcacgaacggtgcaaccgtaatccaatcacccggg	fw	
CdChdC_Y135A	cccgggcgattggattacggttgaccgttcgtgcgc	rev	
CdChdC_W183Y	gcctcaaaccgagcatatactcataatcacccagtgc	rev	W183YY135W
CdChdC_W183Y	gcactgggtgattatgagtatatgctggcggttgaggc	fw	
CdChdC_Y135W	cgcacgaacggcacaaccgtaatccaatcgcccg	rv	
CdChdC_Y135W	cgggcgattggattacggtttggccgttcgtgcg	fw	
CdChdC_T172A	ctgacgtccgtgcaaatgccgtgccgg	fw	T172A
CdChdC_T172A	ccggcacggcatttgacggacgtcag	rv	

CdChdC_T172A	ctgacgtccgtgcaaatgccgtgccgg	fw	T172AY135A
CdChdC_T172A	ccggcacggcatttgacggacgtcag	rv	
CdChdC_Y135A	gcgcacgaacggtgcaaccgtaatccaatcaccggg	fw	
CdChdC_Y135A	ccggggcgattggattacggttgcaccgttcgtgcgc	rev	T172AW183Y
CdChdC_T172A	ctgacgtccgtgcaaatgccgtgccgg	fw	
CdChdC_T172A	ccggcacggcatttgacggacgtcag	rv	
CdChdC_W183Y	gcctcaaaccagcatatactcataatcaccagtc	rev	
CdChdC_W183Y	gcactgggtgattatgagtatatgtggcggttgaggc	fw	T172AY135AW183Y
CdChdC_T172A	ctgacgtccgtgcaaatgccgtgccgg	fw	
CdChdC_T172A	ccggcacggcatttgacggacgtcag	rv	
CdChdC_W183Y	gcctcaaaccagcatatactcataatcaccagtc	rev	
CdChdC_W183Y	gcactgggtgattatgagtatatgtggcggttgaggc	fw	T172AW183YF187T
CdChdC_Y135A	gcgcacgaacggtgcaaccgtaatccaatcaccggg	fw	
CdChdC_Y135A	ccggggcgattggattacggttgcaccgttcgtgcgc	rev	
CdChdC_T172A	ctgacgtccgtgcaaatgccgtgccgg	fw	
CdChdC_T172A	ccggcacggcatttgacggacgtcag	rv	T172AY135AW183YF187T
CdChdC_W183YF187T	cgcgagcctcagtcgacgcatatactcataatcaccagtgcaaac	fw	
CdChdC_W183YF187T	gtttgcactgggtgattatgagtatatgtggcgactgaggctccgcg	rw	
CdChdC_T172A	ctgacgtccgtgcaaatgccgtgccgg	fw	
CdChdC_T172A	ccggcacggcatttgacggacgtcag	rv	
CdChdC_W183YF187T	cgcgagcctcagtcgacgcatatactcataatcaccagtgcaaac	fw	
CdChdC_W183YF187T	gtttgcactgggtgattatgagtatatgtggcgactgaggctccgcg	rw	
CdChdC_Y135A	gcgcacgaacggtgcaaccgtaatccaatcaccggg	fw	
CdChdC_Y135A	ccggggcgattggattacggttgcaccgttcgtgcgc	rev	

To dissolve the delivered primers, 10 × the volume of the given primer concentration of RO-water was admixed, and the sample was placed at 60°C at 500 rpm for 15 min. Subsequently, the primer was 1:10 diluted. This dilution was stored at -30°C to be used as a stock for further processing.

### 3.1.3 Site directed mutagenesis (SDM)

The site directed mutagenesis, to exchange single or multiple amino acid residues, was performed using the QuikChange Lightning Site Directed Mutagenesis Kit provided by Agilent technologies. For an optimal result, the protocol recommended a template DNA concentration of 90 ng/μL.

The reaction mix for 20 μL was set up as follows:

**Table 2:** Composition of the reaction mix used for site directed mutagenesis.

<b>Volume [<math>\mu</math>L]</b>	<b>Ingredient</b>
2	10 $\times$ reaction buffer
1	dsDNA template
0.5	Primer 1
0.5	Primer2
0.4	dNTP mix
0.6	Quik solution reagent
0.4	Quikchange lightning enzyme
15	H2O

Subsequently, the reaction mix was placed into the thermocycler and the cycling parameter were set as follows:

**Table 3** Cycling parameters applied for the performance of the PCR for DNA amplification.

<b>Segment</b>	<b>Cycles</b>	<b>Temperature</b>	<b>Time</b>
1	1	95°C	2 minutes
2	18	95°C	2 seconds
		60°C	10 seconds
		68°C	3:30 minutes
3	1	68°C	5 minutes

After completion of the PCR 0.8  $\mu$ L of DpnI enzyme was added to the reaction mix. The sample was placed on 37°C for 5 min to allow the digestion of parental DNA.

### 3.1.4 Heat-shock transformation of *E. coli* expression strain

5  $\mu$ L of the digested PCR product was then added to a 50  $\mu$ L aliquot of heat-shock competent *E.coli* Tuner (DE3) cells. Additionally, a negative control, lacking the PCR product, was set up. The samples were gently mixed and then placed on 42°C for 45 s for heat shock transformation. Subsequently, the samples were transferred to ice for 2 min. Then 1 mL of LB medium was added to the cells. The cells were let to incubate at 37°C for 1 hour for regeneration. After incubation, the samples were centrifuged for 1min at 10 000 rpm. The

supernatant was discarded. The remaining liquid was spun down again. The cell pellet was resuspended and the remaining ~100  $\mu\text{L}$  of cell suspension were transferred onto pre-tempered (37°C) LB-Kan agar plates. The liquid was distributed with the help of sterile glass beads to obtain single colonies after overnight incubation at 37°C.

*Table 4: Composition of LB-Kanamycin agar.*

LB-Kanamycin Agar	
<b>Ingredient</b>	<b>Concentration</b>
Yeast extract	5 g/L
NaCl	10 g/L
Peptone	10 g/L
Agar	15 g/L
1000 $\times$ Kan	1 ml/L

### 3.1.5 Isolation of the SDM product

On the consequent day, 3 single colonies were picked and each transferred into 4 mL of fresh LB-Kan medium. The cultures were placed at 37°C overnight, shaking at 180 rpm. The next day, 2 mL of the culture was harvested and transferred into 2mL Eppendorf reaction tubes. The samples were centrifuged at 10 000 rpm and the supernatant was discarded. The cell pellet was retained and further processed with the help of the Monarch Plasmid Miniprep Kit to isolate the plasmid DNA from the cells.

The cell pellet was resuspended in 200  $\mu\text{L}$  plasmid resuspension buffer. The sample was vortexed until all cells were completely resuspended. Then 200  $\mu\text{L}$  of plasmid lysis buffer was added. The sample was homogenized by gently inverting the tube for 5-6 times. The sample was let to incubate 1 min at room temperature. 400  $\mu\text{L}$  of plasmid neutralization buffer was added and again the sample was gently inverted and let to incubate at room temperature for 2 min for precipitate formation. The lysate was then centrifuged for 5 min at 13 000 rpm. The supernatant was transferred to the provided spin column for immobilization of DNA to the column matrix. The sample was centrifuged for 1 min at 13 000 rpm. The flow-through was discarded. 200  $\mu\text{L}$  of plasmid wash buffer 1 was added and the sample was centrifuged for 1 min at 13 000 rpm. Then 400  $\mu\text{L}$  of plasmid wash buffer 2 was added and the sample was again centrifuged for 1 min at 13 000 rpm. Subsequently the spin column was transferred in to a clean 1.5 mL reaction tube. 30  $\mu\text{L}$  of MQ- $\text{H}_2\text{O}$  was added to the centre of the matrix. A last

centrifugation step was performed at 13 000 rpm for 1 minute to eluate the plasmid DNA from the spin column.

### 3.1.6 Determination of SDM product concentration

The plasmid concentration of the eluate was determined with the help of the Denovix Nanodrop device. Therefore, the device was first blanked with HP-H<sub>2</sub>O. Then 1 µL of the eluate was added onto the optical sensor and the absorbance at 260 nm was measured, which is proportional to the DNA concentration of the sample.

### 3.1.7 Verification of SDM product

To verify the product of the SDM the sequence of the eluted plasmid DNA was determined by Sanger sequencing at Microsynth. Therefore, the plasmid DNA was diluted to a concentration of 80 ng/µL in a sample volume of 12 µL. For a successful sequencing reaction, sequencing primers are required, which were stored at Microsynth and therefore were added by Microsynth before starting the sequencing process.

The sequencing result was matched with the designed primer sequence for the corresponding variant and checked for sequence identity using SnapGene Viewer.

*Table 5* List of primers, used for the verification of the SDM products

Sequencing primers	
<b>Sequence</b>	<b>Designation</b>
GGTTTCCCTCTAGAAATAATTTTGT	Sequencing_pD441_forward
TAGGGAAGTCCAGGCATCAAATAA	Sequencing_pD441_reverse

### 3.1.8 Cryo cultures

For long-time storage, 2 mL of an overnight culture of the verified target culture was harvested. The cell suspension was centrifuged for 1 min at 10 000 rpm. The supernatant was

discarded and the cell pellet was resuspended in 1 mL of LB medium with 30% of glycerol as cryo-protectant. The culture was then transferred into a cryo-tube and stored at -80°C.

### 3.2 Recombinant expression and purification of *CdChdC* variants

#### 3.2.1 Test expression

To confirm the functionality of the expression system a test expression was carried out. For this purpose, two overnight culture for one *CdChdC* variant was set up. Therefor 20 mL of LB-Kan medium was inoculated with cryo culture of the desired variant. The overnight culture was then inoculated overnight at 37°C with agitation at 180 rpm. The next day, 100 µL of the overnight culture was transferred into 50 mL of fresh LB-Kan medium. The cultures were incubated at 37°C for 3 h at 180 rpm until the culture reaches an OD of 0.6. To check the optical density of the cultures, an aliquot was withdrawn and transferred into a plastic cuvette. The OD was determined at 600nm. After 3 h of incubation the temperature was lowered to 16°C. After another hour of incubation, one the two samples was induced by the addition of 25 µL of 1 M IPTG. Both samples were incubated at 16°C overnight, shaking at 180 rpm. The subsequent day, 2 mL of each cell cultures were harvested and transferred into a fresh 2ml reaction tube. The sample was centrifuged for 15 min at 13 000 rpm for 1 min. The supernatant was discarded and the cell pellet was resuspended in 1 mL of lysis buffer. Additionally, a PCR tube of small glass beads were added. The sample was vortexed twice for 1 min. The sample was again centrifuged at 14 000 rpm at 4°C for 20 min. A 15 µL aliquot of the supernatant was transferred into a fresh reaction tube. 5µL of Laemmli sample buffer was added. Then 10 µL of the sample were loaded onto a precast stain-free gel from BioRad. As a reference the precision plus protein unstained standard was also applied onto the gel. The electrophoresis was driven at 250 V for 20 min.

#### 3.2.2 Expression of *CdChdC* variants in Tuner (DE3) cells and cell harvest

For recombinant production of the target protein 30 mL of LB-Kanamycin (100 µg/mL) medium was inoculated with cryo culture of the desired protein and incubated overnight at 37°C, shaking at 180rpm. The consequent day, 1.5 mL of overnight culture was transferred into 750

mL of fresh LB- medium to which 750  $\mu$ L of a 1000  $\times$  Kanamycin stock was admixed. The culture was incubated for 3 hours at 37°C, shaking at 180 rpm until the culture has reached an OD<sub>600</sub> of  $\sim$  0.6, which was checked with the help of a photometer. After reaching the desired OD<sub>600</sub>, the temperature was lowered to 16°C. After 1 h of incubation at reduced temperature, 375  $\mu$ L of 1 M Isopropyl- $\beta$ -D-thiogalactopyranosid (IPTG) was added to the culture to induce the expression of the desired protein. The culture was incubated over-night at 16°C, shaking at 180 rpm.

On the consequent day, the cells were harvested by centrifugation at 4500 rpm at 4°C for 25 min with an SLA-3000 rotor. The obtained cell pellet was transferred into sterile Falcon tubes and stored at -30°C.

**Table 6:** Composition of LB-Medium

Luria-Bertani medium	
<i>Ingredient</i>	<i>Concentration</i>
Yeast extract	5 g/L
NaCl	10 g/L
Peptone	10 g/L

**Table 7:** Concentration of Antibiotics stock

Antibiotics	
<i>Ingredient</i>	<i>Concentration</i>
1000 $\times$ Kanamycin	50 mg/mL

**Table 8:** Concentration of IPTG stock

Isopropyl- $\beta$ -D-thiogalactopyranosid	
<i>Ingredient</i>	<i>Concentration</i>
IPTG	1 M

### 3.2.3 Cell lysis

To release the target protein the thawed cell pellet from approximately 1.8 L culture was solved in Lysis buffer. Lysis buffer was added until a homogenous but viscous cell suspension was obtained. The cell suspension was then sonicated several times for 90 s at an amplitude of 95 % until a watery fluid was obtained. The sample was then centrifuged with the help of a SS-34 rotor at 18 000 rpm for 25 min at 4°C. The obtained cell debris was discarded while supernatant was filtered with a vacuum pump through a 0.45  $\mu$ M filter paper.



**Table 9:** Lysis buffer composition

Lysis Buffer	
<i>Ingredient</i>	<i>Concentration</i>
Phosphate buffer, pH 7.4	50 mM
NaCl	500 mM
Glycerol	5 %
Triton × 100	0,50 %

### 3.2.4 Metal chelate affinity chromatography

To obtain the target protein a His-Trap column, packed with Ni-sepharose resin, was used. The affinity chromatography was carried out with the help of a BioRad FPLC system. First, the BioRad systems were purged. Then the whole system was flushed with MQ-H<sub>2</sub>O and binding buffer at a flow rate of 10 mL/min. Then the flow-rate was lowered to 0.5 ml/min to insert the column using the drop-on-drop method. The column was then equilibrated with MP-H<sub>2</sub>O followed by binding buffer at a flow rate of 5 ml/min. Subsequently the filtered sample was loaded onto the His-column with a flow rate of 1 ml/min. After this loading step the column was washed with binding buffer at flow rate of 5 mL/min until the absorbance at 280 nm reaches baseline. Then, the column was equilibrated with prescission cleavage buffer at a flow rate of 5 ml/min. After this equilibration step, the flow rate was lowered to 0.5 mL/min to remove the column from the BioRad system. After the loading of the sample was completed the FPLC system was flushed with water and 20 % EtOH, in which it is stored.

15 µL of Prescission HRV C3 protease was dissolved in 6 mL of cleavage buffer. The mixture was then manually loaded onto the column with the help of a syringe. The column was placed at 4 °C for incubation overnight. On the consequent day the protein was eluted by the manual application of 8 mL of SEC-buffer with a syringe.

**Table 10:** Binding buffer composition

Binding Buffer	
<i>Ingredient</i>	<i>Concentration</i>
Phosphate buffer, pH 7,4	50 mM
NaCl	500 mM

**Table 11:** Cleavage buffer composition

Precision Cleavage Buffer	
<i>Ingredient</i>	<i>Concentration</i>
TRIS-HCl, pH 7.0	50 mM
NaCl	150 mM
EDTA	1 mM

### 3.2.5 Quality control of protein purification

To check the purity of the obtained protein and also the efficiency of the metal chelate affinity chromatography an aliquot of the sample was drawn before it was loaded onto the His-Trap column. This aliquot was compared to an aliquot, which was drawn from the flow-through of the sample after passing the His-Trap column. Both aliquots were diluted 1:10 and 1:100. 5  $\mu$ L of Laemmli sample buffer were added to 15  $\mu$ L of the undiluted sample and both dilutions. The samples were then transferred onto a precast, stain-free gel from BioRad. The electrophoresis was driven under the same conditions as already described in 3.2.1.

### 3.2.6 Concentration of eluate and determination of protein concentration

The eluate was collected in an Amicon centrifugal filter unit with a molecular weight cut-off of 50 000 Da. The eluate was centrifuged at 3900 g for 12 min at 4°C. The sample was stored at -80°C.

### 3.2.7 Size exclusion chromatography

As a second purification step, to remove possible formed aggregates, a size exclusion chromatography was performed. Therefore, a HiLoad<sup>TM</sup> 16/600 Superdex<sup>TM</sup> 200 pg column was used on the BioRad FPLC system. The SEC column was equilibrated overnight with SEC buffer with a flow rate of 1 ml/min. After equilibration the sample was loaded onto the column via a sampleloop with a flow rate of 1 ml/min. The process was monitored by measuring the absorbance at 280 nm. As soon as the absorbance started to increase fractions were collected. Relevant fractions were then pooled into an Amicon centrifugal filter unit. The sample was then concentrated by a centrifugation step at 3900 g at 4°C for 12 min. The concentration was then determined by measuring the absorbance at 280 nm. With the help of Lambert Beer's Law and the molecular extinction coefficient of 43 430 M<sup>-1</sup>cm<sup>-1</sup>. The protein stock was then aliquoted in 20  $\mu$ L and stored at -80°C.

**Table 12:** SEC-buffer composition

SEC-Buffer	
<i>Ingredient</i>	<i>Concentration</i>
Phosphate buffer, pH 7.4	100 mM
NaCl	100 mM

### 3.3 Biochemical and biophysical characterization methods

#### 3.3.1 Coproheme titration

To investigate the binding capacity of the *CdChdC* and to determine the molecular extinction coefficient a coproheme titration was carried out. The molecular extinction coefficient is an intrinsic property of a protein and reflects its ability to absorb light at a certain wavelength.

The coproheme titration was carried out in the Cary 60 spectrometer from Agilent technologies. The binding of the coproheme was followed by a wavelength scan between 750 nm and 250 nm at medium scanning velocity (600 nm/min). The assay was performed in a stirred quartz cuvette, with a pathlength of 1 cm and a temperature of 25°C. The spectrum of pure 50 mM phosphate buffer was recorded and used as a baseline.

For this assay 10 µM of *CdChdC* were diluted in 50 mM phosphate buffer (pH 7.4) in a final volume of 1 mL to which 1 µM aliquots of coproheme were admixed in a stepwise manner. The coproheme aliquots were taken from a 3.9 M coproheme stock solution.

At first, the spectral properties of pure *CdChdC* were recorded. Then, after the addition of each aliquot of coproheme, a wavelength scan was performed until no change in the captured spectrum was visible.

#### 3.3.2 Hydrogen peroxide titration followed by UV-vis spectroscopy

A hydrogen peroxide titration was performed to test the functionality of the *CdChdC*, as hydrogen peroxide acts as a sparking agent of the decarboxylation reaction. The titration was carried out in the Cary 60 photometer from Agilent technologies. The reaction was followed by a wavelength scan between 750 nm and 250 nm at medium scanning velocity of 600 nm/min.

For this assay 10  $\mu\text{M}$  of *CdChdC* and 5  $\mu\text{M}$  coproheme were directly diluted in 50 mM phosphate buffer (pH 7.4) to a final volume of 1 mL. A 1 mM hydrogen peroxide stock solution was freshly prepared from which 1  $\mu\text{L}$  aliquots were withdrawn and stepwise added to the reaction mix. The assay was performed in a quartz cuvette, with a pathlength of 1 cm, at 25°C and constant stirring. Before measuring, the spectrum of pure 50 mM phosphate buffer (pH 7.4) was recorded and used as a baseline.

At first, a spectrum was recorded of the coproheme-*CdChdC* complex without the addition of hydrogen peroxide. Then, hydrogen peroxide was added in 1  $\mu\text{M}$  steps until a final hydrogen peroxide concentration of 50  $\mu\text{M}$  was reached. After each addition of hydrogen peroxide, a spectrum was recorded.

### 3.3.3 Chlorite titration followed by UV-vis spectroscopy

Hydrogen peroxide, the natural substrate of the *CdChdC* is known to be a two-electron donor. As an alternative two-electron donor sodium chlorite can be used to initiate the decarboxylation reaction performed by the *CdChdC*. Hydrogen peroxide has to undergo a deprotonation step prior to electron transfer, which is not the case for sodium chlorite.

Chlorite titration followed by UV-vis spectroscopy was carried out under the same conditions and settings as already described in [3.3.2](#), except for the preparation of  $\text{NaClO}_2$ . 10 mL of a 10 mM  $\text{ClO}_2^-$  stock solution were prepared. This stock solution was diluted 1:10. The exact concentration of the working stock was determined with the help of a photometer and the molecular extinction coefficient of  $154 \text{ M}^{-1}\text{cm}^{-1}$  at 260 nm.

### 3.3.4 Steady-state kinetics

Investigation of steady-state kinetics was performed to determine the enzymatic activity and the effect of the introduced mutations. With the help of steady-state kinetics, initial reaction rates were determined. Therefore, the course of the reaction was monitored photometrically at a distinct wavelength for 120 s using the Chirascan circular dichroism spectrophotometer from Applied Photophysics (Leatherhead, UK).

Before measuring, the Chirascan was flushed with Nitrogen with a flow rate of 5 ml/min for 30 min. The the UV-lamp was let to initialize for another 30 min. The measurement was performed at a wavelength of 392 nm and a bandwidth of 1 nm. For this assay a protein stock solution with an enzyme concentration of 10  $\mu$ M and a coproheme concentration of 5  $\mu$ M were prepared. The components were diluted in 250 mM phosphate buffer (pH 7.4). A hydrogen peroxide stock solution of 1 mM was prepared. The reaction was performed in a stirred quartz cuvette in a final volume of 1 mL. Before measuring, 200  $\mu$ L of protein stock solution and 800  $\mu$ L of water were mixed together and recorded as a blank.

For each reaction mix, at first, water was added to the cuvette in varying volumes, depending on the desired hydrogen peroxide concentration. Then 200  $\mu$ L of the protein stock solution was added. As final ingredient hydrogen peroxide was admixed in varying concentrations between 0  $\mu$ M and 100  $\mu$ M. The measurement was immediately started after the addition of hydrogen peroxide. Each concentration was measured in triplicates, which were baseline corrected and averaged. With the help of the ProDataViewer Software, the curves were evaluated and the initial slope of the reaction was obtained.

### 3.3.5 Pre-steady state kinetics

Pre-steady state kinetics observes and studies enzyme behaviour within the first milliseconds after the enzyme is mixed with the substrate or a ligand. A suitable method to follow this short, initial time span is stopped-flow UV-vis spectroscopy. In stopped-flow spectroscopy, two reactants are prepared in separate syringe reservoirs. A defined volume of both components is released into the measurement cell, in which the solutions are mixed. The reaction progresses until, the stop syringe reservoir is filled. When the reservoir of the stop syringe is completely filled, the syringe hits a trigger on a block and the flow as well as the reaction is stopped.

All experiments were performed using the Stopped- Flow devices SX-18MV or  $\pi$ -Star equipped with a diode array detector or a photomultiplier (Applied Photophysics). Conventional stopped flow technique was performed by mixing two components; enzyme and substrate. Besides investigation of pre-steady state kinetics with hydrogen peroxide, the reaction with HCN was examined.

Prior to measurement, 10  $\mu\text{M}$  of *CdChdC* and 4  $\mu\text{M}$  of coproheme were prepared in 2.5 mL of 50 mM phosphate buffer (pH, 7.4). Concentrations of hydrogen peroxide and HCN were selected between 200  $\mu\text{M}$  and 1000  $\mu\text{M}$ . The change in absorbance was monitored at 393 nm. The obtained time traces were analysed and fitted with a single exponential fit, using the ProDataViewer software. With the help of the ProDataViewer software, observed rate constants  $k_{\text{obs}}$  were obtained. The  $k_{\text{obs}}$  values were plotted against substrate concentrations. With the help of this linearized plot, values for the apparent binding constants ( $k_{\text{on}}$ ) and the dissociation constants ( $k_{\text{off}}$ ) were calculated. The apparent binding constants ( $k_{\text{on}}$ ) was obtained from the slope of the plot and the dissociation constants ( $k_{\text{off}}$ ) determined by the calculation of the y- intercept. The  $K_{\text{D}}$  value was obtained by dividing  $k_{\text{off}}$  by  $k_{\text{on}}$ .

### 3.3.6 Electronic circular dichroism

To investigate the configuration and conformation of the molecular structure of the wild-type enzyme and its variants, electronic circular dichroism (ECD) spectroscopy was applied. ECD measurement is based on the ability of a chiroptical substance to differentially absorb left- and right circularly polarized light. Besides information on the secondary structure of a sample, ECD can be used to obtain insight in the thermostability of a sample by the application of a temperature gradient.

Furthermore, the apo-form of the protein is compared to coproheme-bound form of the protein to examine the influence of the cofactor on the secondary structure.

Spectral scans were taken in the near UV-region between 260 nm and 500 nm as well as in the far UV region between 250 nm and 190 nm using the Chirascan from Applied Photophysics (Leatherhead, UK). The instrument was prepared as described in [3.3.4.](#)

To obtain far UV-spectra 5  $\mu\text{M}$  of the apo *CdChdC* was diluted in 300  $\mu\text{L}$  of 5 mM phosphate buffer (pH 7.4). The mix was then transferred into a small, quartz cuvette with a path length of 1 mm. The sample was then analysed between 180 and 250 nm, at 20°C. A scanning time of 10 s for each wavelength was chosen. For analysis of the coproheme bound-form of the proteins, 5  $\mu\text{M}$  *CdChdC* and 5  $\mu\text{M}$  of coproheme were admixed in 300  $\mu\text{L}$  of 5 mM phosphate buffer. The samples were analysed as previously described.

For near UV measurement, the samples were prepared as described for the far UV region. Spectra were recorded between 260 nm and 500 nm. The scanning parameter were set identical as for the far UV measurement.

Unfolding studies were performed at a single wavelength of 393 nm. 5  $\mu$ M of *CdChdC* and 5  $\mu$ M of coproheme were prepared in 300  $\mu$ L of 50 mM phosphate buffer (pH 7.4). The sample was transferred to quartz cuvette (path length: 1 mm), which was closed with a lid and a temperature sensor was applied. An initial spectrum at 20°C was taken. Then a temperature gradient to 80°C was applied to the sample, which increased with a rate of 1°C/min. At 80°C, a spectrum of the unfolded protein was recorded. To observe potential refolding of the protein, the temperature was lowered to 20°C and a spectrum was taken. The obtained temperature curve was then analysed with the help of the ProDataViewer. The curves were analysed using sigmoid fits to obtain values for the melting temperature of each variant.

### 3.3.7 MNP spin trapping

The formed tyrosyl radical during the decarboxylation reaction with hydrogen peroxide was caught and identified with the help of the MNP (2-methyl-2-nitrosopropane) spin trapping assay. MNP is known to specifically attack tyrosyl radicals and convert them into 3-nitrotyrosine. This conversion results in an increase of molecular mass by +44.98 Da, which was detected by mass spectrometry (27).

5 mg of MNP were dissolved in 100  $\mu$ L of water at 60°C for 30 min in the absence of light. 60  $\mu$ M of *CdChdC* and 30  $\mu$ M of coproheme were dissolved in 50 mM phosphate buffer. For each variant a reaction series, with a final volume of 100  $\mu$ L, and 4 different hydrogen peroxide concentrations between 0  $\mu$ M and 2400  $\mu$ M, was set up. 10  $\mu$ L of the MNP stock solution were added to each of the samples.

For peptide analysis the samples were digested in gel. The proteins were S-alkylated with iodoacetamin and trypsin digested. The samples were then loaded on a nanoEase C18 column (nanoEase M/Z HSS T3 Column, 100Å, 1.8  $\mu$ m, 300  $\mu$ m X 150 mm, Waters). 0.1% formic acid was used as an aqueous solvent. The peptides were eluted by a gradient from 3.5% B (B: 80% ACN, 20% A) to 95% B with a flow rate of 6  $\mu$ L/min. The 8 most prominent peaks were selected for fragmentation.

The detection of the peptide was performed with the help of an iontrap mass spectrometer (amazon speed ETD, Bruker) equipped with the standard ESI source in positive ion, data dependent acquisition (DDA) mode, which includes a switch to MSMS mode for eluting peaks. MS scans were recorded within the range of 150-2200 Da.

### 3.3.8 MALDI-TOF mass spectrometry

Matrix-assisted laser desorption ionization (MALDI) time of flight (TOF) is a mass spectrometry method which can be used to accurately identify the mass of proteins or other organic substances like heme and its derivatives.

Upon MALDI analysis, the sample is ionized by a laser, which splits up large molecules into fragments. The MALDI sample is treated with a volatile matrix prior to analysis, which acts as a laser energy absorbent. The mixture is then spotted on a metal plate. When the laser is directed onto the sample, the solid phase evaporates upon ion formation. The generated gaseous ions are accelerated and separated according to their mass/charge ratio.

For MALDI analysis 10  $\mu\text{M}$  of CdChdC and 5  $\mu\text{M}$  of coproheme are diluted in 50 mM phosphate buffer (pH 7.4). For each variant, a reaction series, with a final volume of 50  $\mu\text{L}$  and six varying hydrogen peroxide concentrations ranging from 0  $\mu\text{M}$  to 200  $\mu\text{M}$  hydrogen peroxide, was set up. The reaction series was then 1:5 diluted. From each of the reaction tubes, undiluted and diluted, an aliquot of 1  $\mu\text{L}$  was withdrawn and transferred into 2  $\mu\text{L}$  of sinapic acid. The mix was homogenized by pipetting up and down. 1  $\mu\text{L}$  of the mix was spotted onto the MALDI target plate.

The samples were then analysed using MALDI Autoflex (Bruker). MS spectra were recorded in a mass range between 500 and 1000 Da to identify heme derivatives by their exact mass.

### 3.3.9 Size exclusion chromatography multiangle light scattering

As a quality control, of the generated variants a SEC-MALS analysis was performed. SEC-MALS is a combination of a size-exclusion chromatography and multi-angle light scattering technology. Size exclusion chromatography is responsible for the separation of the different



fractions within a sample according to their molecular weight. Subsequently, the exact molecular mass of the eluted samples was determined with MALS. MALS is based on the ability of a sample to scatter light from a laser to a certain degree which corresponds to the molecular mass or the average size of molecules in solution.

For SEC-MALS analysis, 100  $\mu\text{M}$  of the apo protein and was prepared in 50  $\mu\text{L}$  1  $\times$  PBS buffer with 100 mM NaCl. For analysis of the coproheme-bound form of the enzyme, 100  $\mu\text{M}$  of *CdChdC* and 100  $\mu\text{M}$  of coproheme were diluted in the same volume of buffer. The samples were centrifuged through a Ultrafree-MC filter with a pore size of 0.1  $\mu\text{m}$  (Merck Millipore) at 10 000 g for 5 min. The flow-through was then transferred into an HPLC vial and placed into the HPLC device. A Superdex 200 10/300 GL column(GE Healthcare) with a pore size of 13  $\mu\text{m}$  was equilibrated with 1  $\times$  PBS with 100 mM NaCl at a flow rate of 0.75  $\mu\text{L}/\text{min}$  prior to sample application. The HPLC system used, was equipped with a RIF-10Av refractive index detector, a photodiode array detector (Shimadzu) and MALS Heleos Dawn8+ with QELY detector (Wyatt Technology).

## 4 Results

### 4.1 CdChdC variants

The first goal of this thesis was the successful generation of CdChdC variants, based on the CdChdC-WT sequence.

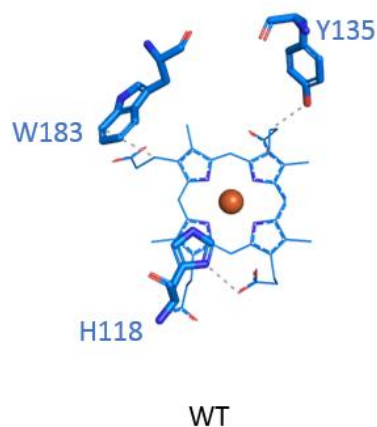


**Figure 10: Active site structure of CdChdC wild-type**

With the help of site directed mutagenesis the following variants have been established, which are described in the next chapters.

#### 4.1.1 Tyrosine swap variants

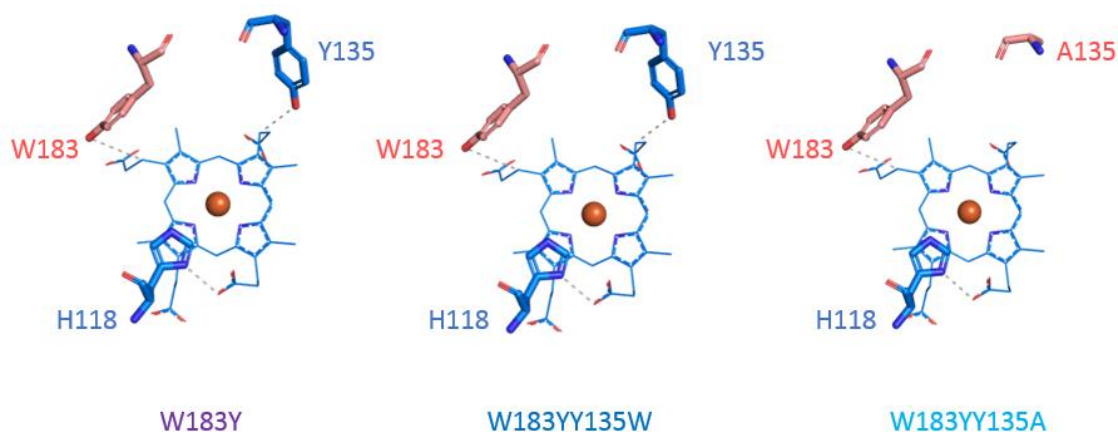


**Figure 11: Active sites of tyrosine swap variants.** Light pink amino acid residue represent the introduced mutations by sited directed mutagenesis in comparison to the WT-active site presented in figure 11.

To investigate the effect of the relocation of the reactive tyrosine 135, a W183Y variant was created. Therefore, the tryptophane on position 183 is replaced by a tyrosine. The resulting variant then carries two tyrosine residues in the proximity of two propionate groups, p2 and p4 respectively, of coproheme. In the W183YY135W variant the amino acids on the respective positions are exchanged to mirror the nature of the active site from propionate p2 to p4. To exclude an artefact reaction of the incorporated tryptophan on position 135, a control variant was established, holding an unreactive alanine on position 135.

#### 4.1.2 Variants, investigating the role of threonine 172

To examine the role of threonine 172, at first the single mutant T172A was established. For this purpose, the threonine on position 172 was replaced by the small and non-reactive amino acid alanine. Beside a divergence in size, threonine and alanine differ in their polarity. Additionally the double mutant T172AY135A was created, lacking the essential, reaction-performing tyrosine. An alanine residue exchanged the tyrosine. The T172AW183Y tries to exploit the variance in hydrophobicity and polarity to facilitate and direct the electron transfer towards the tyrosine 183. The triple mutant T172AY135AW183Y solely holds a tyrosine on position 183 to test the decarboxylation potential of the tyrosine located in the vicinity of propionate p4.

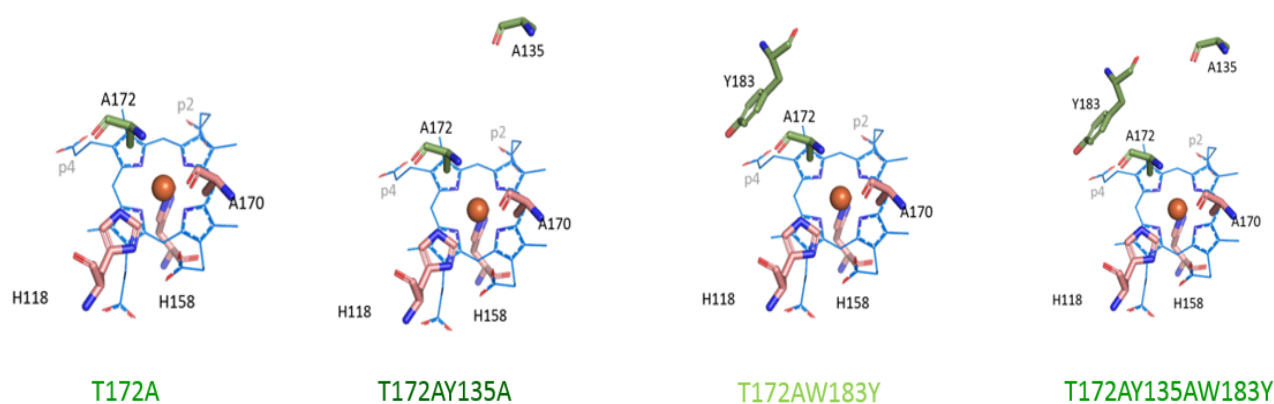


**Figure 12: Active sites of variants, established for the investigation of threonine 172.** Light green coloured amino-acids represent the introduced mutations by site-directed mutagenesis in comparison to the WT-active site presented in Figure 11.

#### 4.1.3 Variants, investigating the role of tyrosine 183

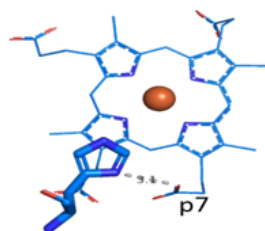


**Figure 13:** Active site of WT-CdChdC, highlighting H118 and its interaction partner propionate 7.

The H118F variant based the fundament for the investigation of tyrosine 183. The pre-existing H118F variant is known for its ability to produce the reaction intermediate MMD due to a steric blockage of the inserted phenylalanine instead of the native histidine. The H118FW183Y variant was designed to investigate the decarboxylation potential of the tyrosine 183. The idea was to repromote the ability to produce heme *b* with the incorporation of a tyrosine near propionate p4. Furthermore, a triple mutant H118FY135AW183Y was generated, lacking the native tyrosine 135.

To check the functionality of the established expression systems a test expression in small scale was performed. The lysate of a non-induced culture is compared to the lysate of an induced culture with the help of a SDS-Page. The results of the SDS-Page are shown in Figure 15.

Lane #1 represents the applied standard and the corresponding molecular weights. A band at ~25 kDa can be spotted in lanes # 3, 5, 7 and 9, which corresponds to the size of the protein of interest. Onto these lanes each, the lysate of the induced culture of the WT and the variants W183Y, W183YY135W and W183YY135A, were applied, indicating the establishment of an effective expression system for each of the variants.

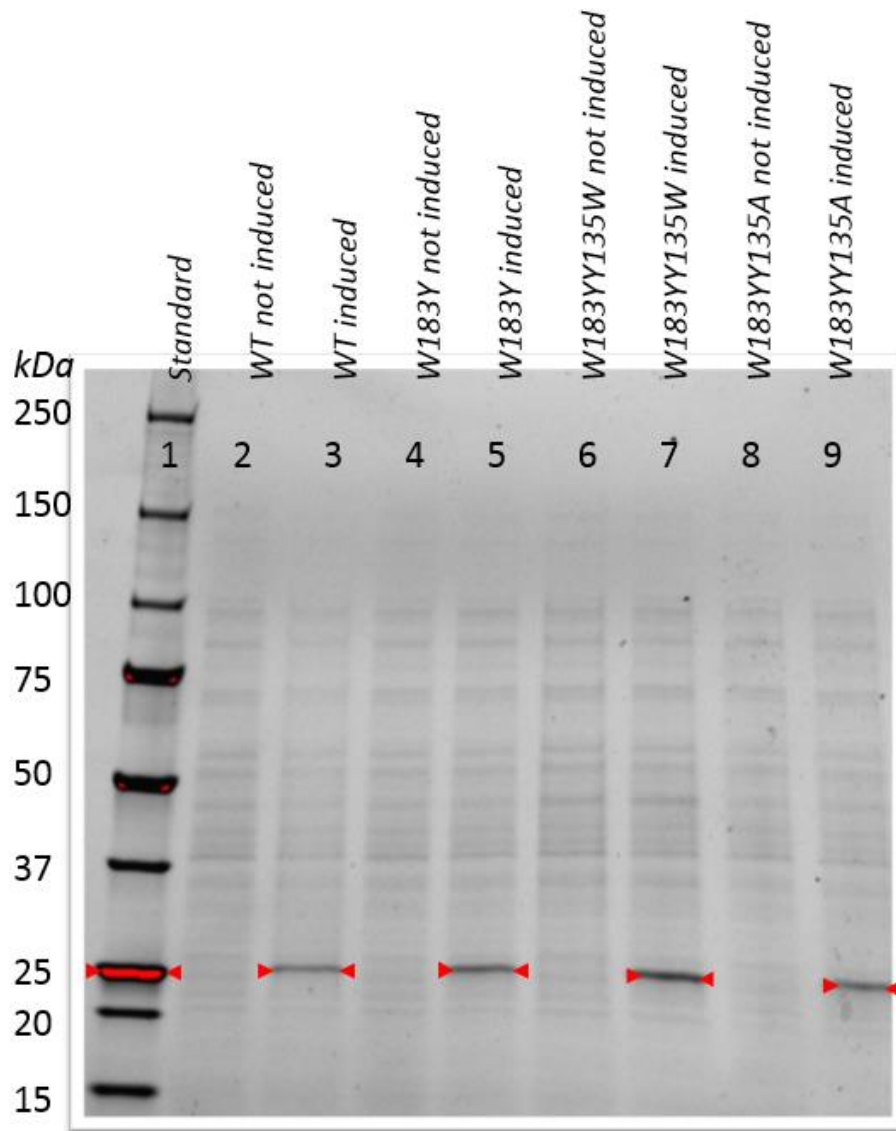


**Figure 14: Illustration of the SDS – page** performed to check the functionality of the established expression systems. Lane#1 represents the lanes of the applied precision plus protein unstained standard with its corresponding molecular weight. Lanes # 2,4,6 and 8 represents the lysate of the non-induced variants whereas lanes # 3, 5, 7 and 9 depicts the induced expression systems. A band at ~ 25kDa in the lane of the induced cultures represents the protein of interest.

The protein of interest was then expressed in large scale, harvested and purified with the help of metal chelate affinity chromatography. Table 13 summarizes the obtained yields of the respective variants after protein purification. The values of the obtained yields range in the same magnitude for constructs with single and double insertions whereas a slight decrease in the yield for constructs with triple insertions can be observed.

**Table 13:** Obtained yields through protein expression and purification.

<b>Variant</b>	<b><i>c</i> [mg/L <i>E. coli</i> culture]</b>
T172A	34.10
T172AY135A	40.20
T172AW183Y	43.80
T172AY135AW183Y	22.15
W183Y	22.61
W183YY135W	54.58
W183YY135A	51.84
H118F	28.22
H118FW183Y	53.83
H118FY135AW183Y	25.62

## 4.2 Size exclusion chromatography multiangle light scattering

As a quality control, to check the purity of the expressed variants, the proteins were analysed by size exclusion chromatography combined with multiangle-light scattering. In figure 13, the chromatograms of the respective variants are summarized. Each chromatogram provides information on the purity of the apo-form (full-line) of the enzyme as well as its holo-form (dashed line). According to figure 16, most variants revealed an almost monomeric peak at a retention time of ~16 min. Minor peaks at a retention time of ~ 10 min, indicate the presence of minor aggregations.

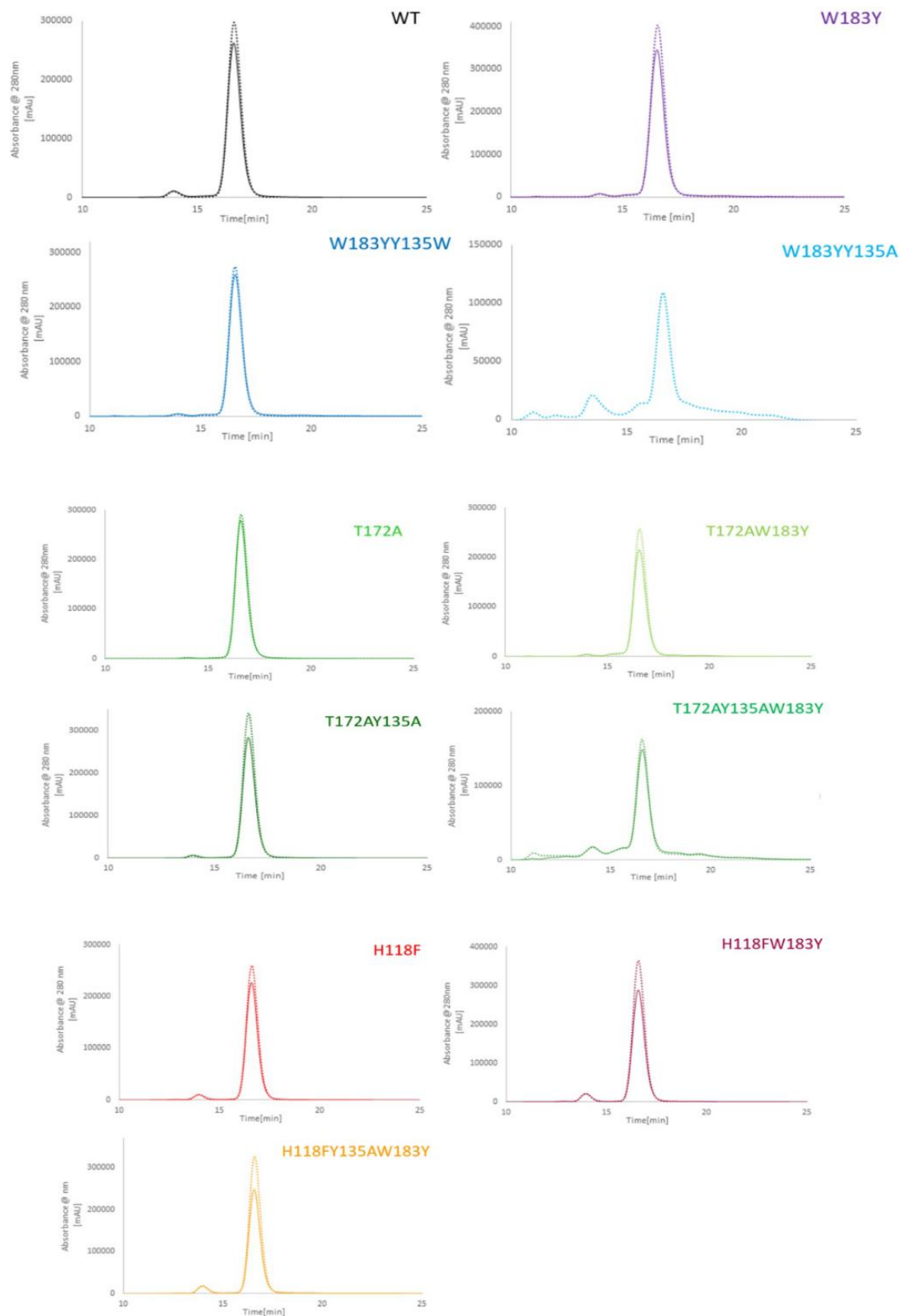


**Figure 15: Chromatograms of HPLC-SEC-MALS analysis.** The full line represents the spectrum of the apo-variants, whereas the dotted line depicts spectral properties of the holo-variants.

### 4.3 Coproheme titration

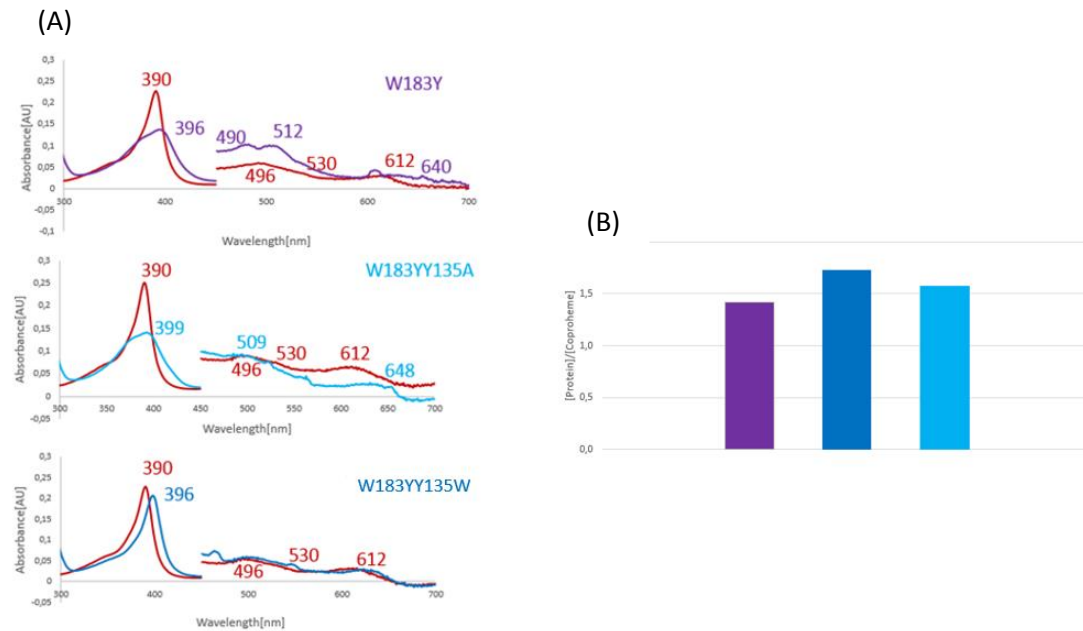


**Figure 16: (A) UV-vis absorption spectra of W183Y (violet), W183YY135W (blue) and W183YY135A (light-blue),** representing the spectral transition induced by the binding of coproheme to the active site of the variants. The red spectrum depicts spectral properties of free coproheme in solution. The purple, light blue and blue spectra illustrate the spectral properties of the fully-occupied active site of the respective variants. (B) Represents the binding capacity of the respective variants, determined by the ratio between the applied concentration of protein to coproheme.

The coproheme titration experiment provides information about the spectral properties of the established mutant in their holo-form (Figure 14A) and information on the binding ability of the variants was obtained. Furthermore, the molar extinction coefficients for the coproheme bound species were determined to be  $\epsilon_{396} = 75822 \text{ M}^{-1}\text{cm}^{-1}$  (W183Y),  $\epsilon_{396} = 120025 \text{ M}^{-1}\text{cm}^{-1}$  (W183YY135A) and  $\epsilon_{396} = 72314 \text{ M}^{-1}\text{cm}^{-1}$  (W183YY135A) with the help of this experiment.

Figure 17A depicts the spectral properties of free coproheme (red) in 50 mM phosphate buffer pH 7.4 with its characteristic Soret maximum at 390 nm. In the visible region, its Q and CT (charge transfer) bands characterize coproheme. A gentle peak at 612 nm indicates the CT band and the shoulder at 530 nm as well as the gentle peak at 466 nm are referred as Q $\alpha$  and Q $\beta$ . With the stepwise addition of the respective variant, the spectral properties alter and migrate towards higher wavelengths.

The holo-W183Y (violet) reveals a Soret Maximum at 396 nm with a characteristic shoulder at 375 nm. In the visible region, the CT band shifts from 612 nm to 640 nm. Q $\alpha$  stays at 530 nm



but interestingly,  $Q_\beta$  significantly change upon the addition of protein. In the holoW183Y the  $Q_\beta$  band shifts to 512 nm and a peak at 490 nm appears.

Holo-W183YY135A (light blue) exhibits a shift in the Soret maximum from 390 to 399 nm. Upon coproheme binding the sharp Soret maximum of the coproheme alters to a broad peak with a characteristic shoulder between 370 nm and 388 nm. The  $Q_\beta$  is affected by a minor red shift from 496 nm to 509 nm. The CT band migrates from 612 nm to 648 nm.

For the W183YY135W variant, the Soret maximum shifts from 390 nm to 396 nm with no alteration in the shape of the peak. Interestingly, the spectrum in the range between 450 nm and 700 nm is barely affected by changes in the spectral properties from free coproheme to the holo-form of W183YW135W.

Furthermore, the molar extinctions coefficients of the respective variants were calculated to obtain information about the ability of each variant to absorb light at a certain wavelength. For proteins, the molar extinction coefficient at 280 nm correlates to the number of aromatic amino acids present, as they are solely capable to absorb light.

Moreover, the coproheme binding capacity was investigated. Therefore, the ratio between the employed protein and coproheme concentration was calculated. It was observed that, the W183Y variant requires a 1.4-fold excess of coproheme for a fully occupied active site. W183YY135A and W183YY135W revealed similar binding capacities, with a protein to coproheme ratio of 1.6 and 1.7 respectively. In principle, the values for the protein to coproheme ratio range in the same magnitude but variants W183YY135A and W183YY135W, carrying two mutations, revealed a slightly elevated ratio compared to the single mutant W183Y.

#### 4.4 Hydrogen peroxide titration followed by UV-vis absorption spectroscopy

To investigate the functionality of the enzymes and their ability to convert the substrate coproheme into heme *b*, a hydrogen peroxide titration assay was performed, as hydrogen peroxide is the natural sparking oxidant for this reaction.

#### 4.4.1 Tyrosine swap mutants

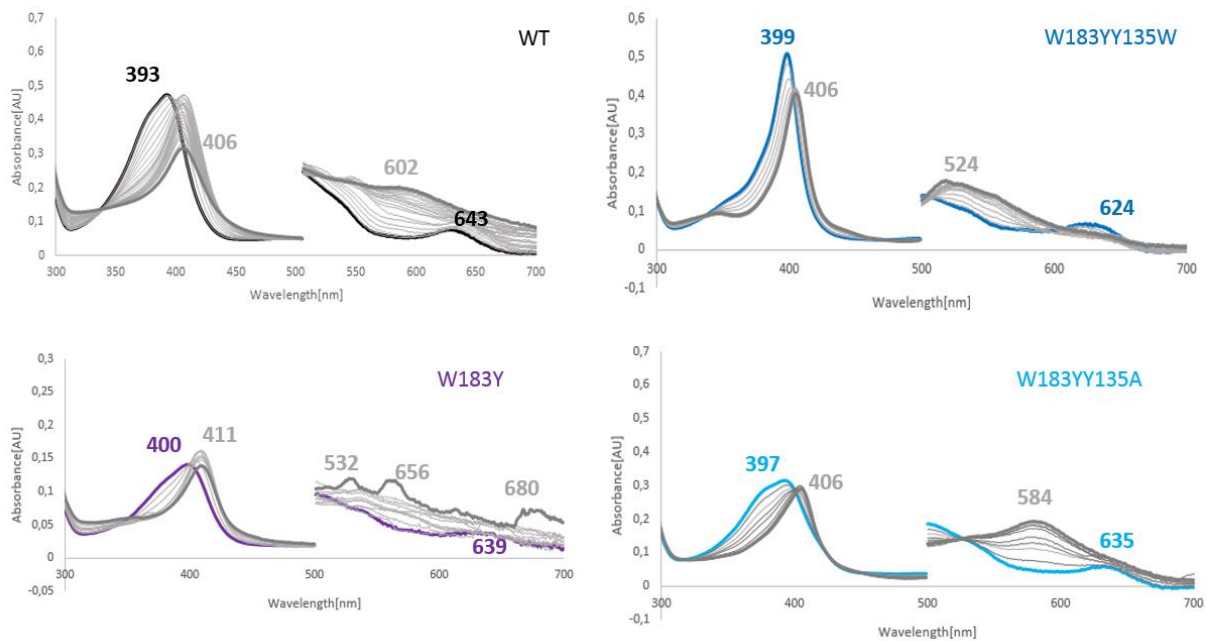


**Figure 17** UV-vis spectra of the WT (black); W183Y (violet); W183YY135W (blue) and W183YY135A (light blue) recorded during hydrogen peroxide titration. The coloured spectra delineate the spectral properties of the coproheme-bound form of each variant, in the absence of hydrogen peroxide. A spectral transition can be followed as hydrogen peroxide is added in 2  $\mu$ M steps, resulting in the terminal, grey spectrum. The spectrum was enlarged by a factor of 5 from 450 nm for a detailed representation of the visible region.

The coproheme-bound form of the WT exhibits an absorption maximum at 393 nm and the CT band at 643 nm as well as the Q-band with maxima at 504 nm and 530 nm. At 393 nm, the peak displays a broad shape with a characteristic, small shoulder between at approximately 375 nm. With an increasing concentration of added hydrogen peroxide, the spectrum shifts to the right terminating at 406 nm. In the visible region, the maxima at 504 nm and 643 nm disappear and a peak at 602 nm arises.

The spectrum of the W183Y variant displays a Soret maximum at 400 nm for its coproheme-bound form, which migrates to 411 nm as hydrogen peroxide is added. In the visible region, the W183Y variant exhibits maxima at 640 nm and 500 nm for its holo-form. In the terminal spectrum, no clear maximum can be identified. The maxima at 532 nm, 656 nm and 680 nm refer to be artefacts induced by stirred agitation.

A sharp, narrow peak characterizes the maximum of holo-W183YY135W at 399 nm. The peak broadens during titration of hydrogen peroxide and the maximum absorption transfers to 406

nm. The CT band at 624 nm disappears with increasing hydrogen peroxide concentration and the Q-band is shifted to 524 nm.

The W183YY135A spectrum reveals a Soret maximum at 399 nm and local maxima in the visible region at 509 nm and 648 nm respectively. Both maxima diminish as the hydrogen peroxide concentration increases, while a prominent and significant peak at 580 nm develops.

#### 4.4.2 Variants, investigating the role of threonine 172

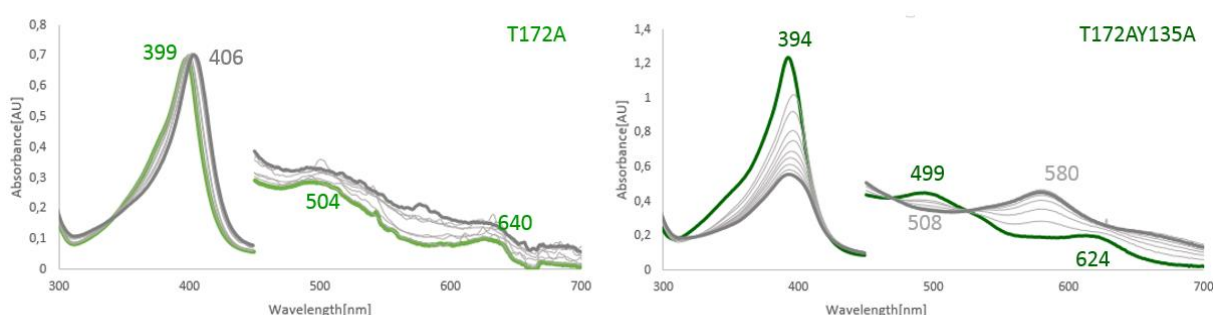


**Figure 18: UV-vis spectra of T172A (light green) and T172AY135A (dark green).** The coloured spectra delineate the spectral properties of the coproheme-bound form of each variant, in the absence of hydrogen peroxide. A spectral transition can be followed as hydrogen peroxide is added in 2  $\mu$ M steps, resulting in the terminal, grey spectrum. The spectrum was enlarged by a factor of 5 from 450 nm for a detailed representation of the visible region.

The T172A variant, exhibits a Soret maximum at 399 nm in its coproheme-bound form. The T172A spectrum reveals the CT band at 640 nm and a Q-band at 504 nm. When hydrogen peroxide is added, a spectral transition takes place and the absorption maximum shifts to 406 nm. Interestingly, in the visible range, no spectral transition can be observed. The maxima remain unaltered, except for their intensity.

The spectrum of the double mutant, T172AY135A, lacking the reactive tyrosine, displays an absorption maximum at 394 nm. This maximum, with increasing substrate concentration stays unaffected. The decrease in absorbance, which can be observed occurs due to heme bleaching. The maximum at 499 nm turns into a minimum at 508 nm whereas the CT band shifts from 624 nm to 580 nm.

#### 4.4.3 Variants, investigating the role of tyrosine 183

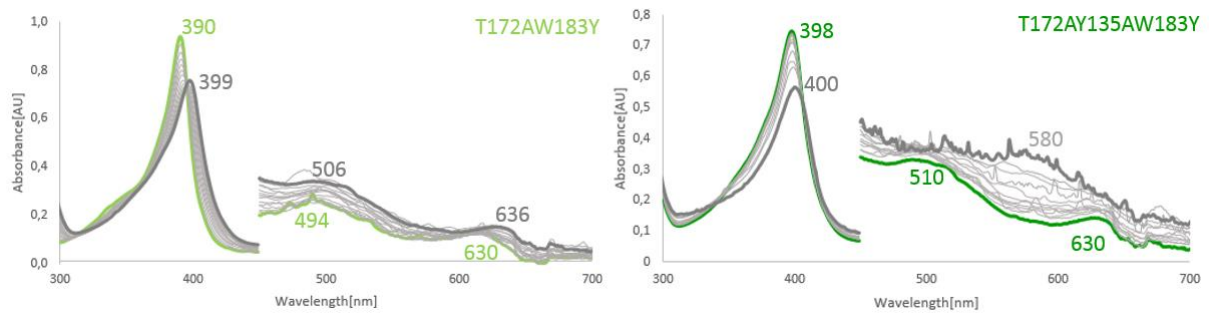


**Figure 19 UV-vis absorption spectra of T172AW183Y (grass green) and T172AY135AW183Y (green).** The coloured spectra delineate the spectral properties of the coproheme-bound form of each variant, in the absence of hydrogen peroxide. A spectral transition can be followed as hydrogen peroxide is added in 2  $\mu$ M steps, resulting in the terminal, grey spectrum. The spectrum was enlarged by a factor of 5 from 450 nm for a detailed representation of the visible region.

Figure 20 depicts the spectral behaviour of the T172AW183Y variant as well as the T172AY135AW183Y variant recorded as hydrogen peroxide is stepwisely added. A sharp, narrow peak at 390 nm characterizes the T72AW183Y mutant as well as two peaks in the visible region. The first is located at 494 nm and the second at 630 nm. Substrate addition induces the migration of the maximum to 399 nm as well as to 506 nm and 636 nm respectively.

The spectrum for the triple variant T172AY135AW183Y displays a small spectral change upon hydrogen peroxide addition by the red-shift from 398 nm to 400 nm. The visible region of the spectrum reveals maxima at 510 nm and 630 nm. Both maxima diminish with the addition of hydrogen peroxide while a prominent and characteristic peak appears at 580 nm.

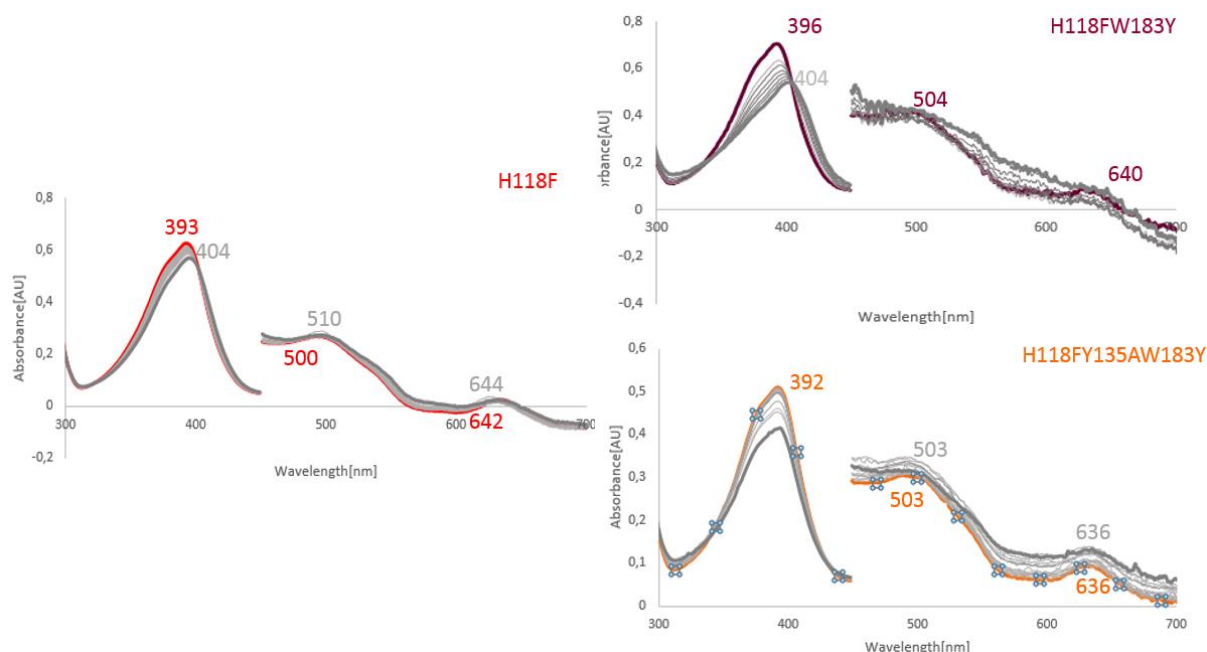


**Figure 20: UV-vis absorption spectra of H118F (red) and H118FW183Y (purple) and H118FY135AW183Y (orange).** The coloured spectra delineate the spectral properties of the coproheme-bound form of each variant, in the absence of hydrogen peroxide. A spectral transition can be followed as hydrogen peroxide is added in 2  $\mu$ M steps, resulting in the terminal, grey spectrum. The spectrum was enlarged by a factor of 5 from 450 nm for a detailed representation of the visible region.

Figure 21 depicts UV-vis spectra of variants H118F, H118FW183Y and H118FY135AW183Y. The H118F single mutant reveals a broad peak at 393 nm with a characteristic shoulder. The absorption maximum shifts to 400 nm in the presence of hydrogen peroxide. The H118F variant is known for its ability to produce MMD. A Soret maximum at 400 nm characterizes the presence of MMD. Furthermore, the H118F variant exhibits maxima at 500 nm and 642 nm. The maxima in the visible region are affected by minor wavelength shift to the right to 510 nm and 644 nm respectively.

The coproheme-bound form of the H118FW183Y results in an absorption maximum at 396 nm indicated by broad peak with a steep slope between 396 nm and 370 nm. The maximum shifts to 406 nm as hydrogen peroxide as substrate is added. In the visible region, the coproheme-bound form of H118FW183Y reveals maxima at 508 nm and 640 nm, which remain almost unaffected.

For the triple variant, H118FY135AW183Y, no spectral transition is observed. The initial spectrum of the coproheme bound variant shows an absorption maximum at 396 nm, remaining unaltered as hydrogen peroxide is added. Solely a decrease in the absorbance is

observed. Maxima at 503 nm and 636 nm characterize triple mutant in the visible range. As well as the maximum at 396 nm, these two remain at their respective position.

## 4.5 Chlorite titration followed by UV-vis absorption spectroscopy

*In vitro* peroxyacetic acid, flavin mononucleotide and sodium chlorite were identified as alternative substrates to launch the reaction (27; 29), thus sodium chlorite titrations were performed, which aimed to investigate the enzymatic behaviour of the variants in the presence of an alternative two-electron donor.

### 4.5.1 Tyrosine swap mutants

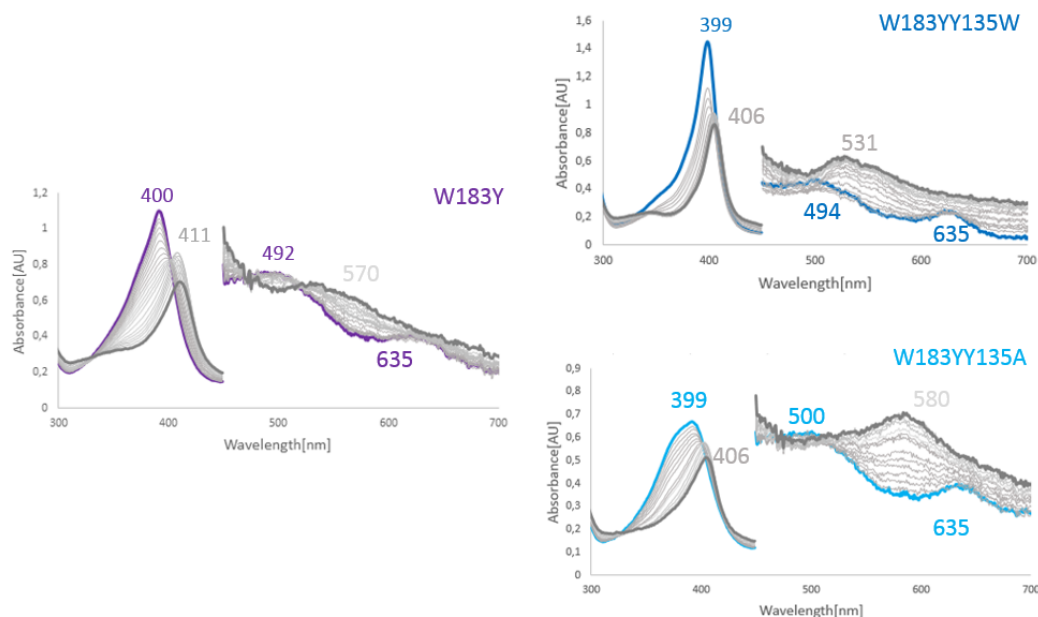


**Figure 21 UV-vis absorption spectra of W183Y (violet); W183YY135W (blue) and W183YY135A (light blue).** Recorded during sodium chlorite titration. The coloured spectra delineate the spectral properties of the coproheme-bound form of each variant, in the absence of the alternative substrate sodium chlorite. A spectral transition can be followed as hydrogen peroxide is added in 2  $\mu$ M steps, resulting in the terminal, grey spectrum. The spectrum was enlarged by a factor of 5 from 450 nm for a detailed representation of the visible region.

The W183Y variant exhibits a Soret maximum of its coproheme bound form at 400 nm, which migrates to the left until it stops at 411 nm, with increasing sodium chlorite concentration. Comparing the spectrum of the hydrogen peroxide titration and the sodium chlorite titration,

no deviations between these spectra are observed within the range of 300 nm and 450 nm. In the visible region the W183Y variant revealed slightly deviating spectral properties as recorded for the hydrogen peroxide titration. The addition of sodium chlorite induced the growth of a maximum at 570 nm. As a comparison, with hydrogen peroxide, maxima at 532 nm, 656 nm and 680 nm appeared.

The spectra of the hydrogen peroxide and the sodium chlorite titration resulted in identical results. The initial Soret maximum of 399 nm shifted to 406 nm. A prominent maximum arose at 580 nm while the CT band at 635 nm as well as the Q-bands at 494 nm and 530 nm vanished.

The same similarity in the spectral behaviour with sodium chlorite and hydrogen peroxide is observed for the W183YY135W variant.

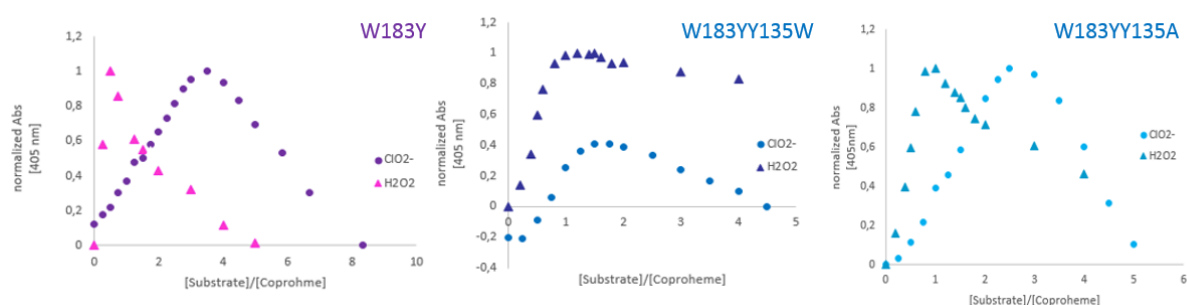


**Figure 22: Comparison of the substrates hydrogen peroxide and sodium chlorite for variants W183Y, W183YY135W and W183YY135A.** The circles represent the the ratio [sodium chlorite/coproheme] plotted against the normlized absorbance at 405 nm. The tringles delineate the ratio [hydrogen peroxide/coproheme] plotted against the normalized absorbance at 405 nm.

In figure 23, the eventual heme *b* formation potential of the variants is displayed. The data of figure 23 will provide quantitative information on the heme *b* formation of the variants in the presence of hydrogen peroxide and sodium chlorite respectively. An increase in the absorbance at 405 nm spectroscopically indication for the formation of heme *b*. Furthermore, figure 20 provides information, which of the two substrates promotes the conversion of coproheme into heme *b* more efficiently.

W183YY135W apparently requires a similar substrate to coproheme ratio with hydrogen peroxide and sodium chlorite for the complete conversion of the available coproheme into heme *b*.

For W183Y and W183YY135A it seems, that the natural substrate hydrogen peroxide promotes a faster and more efficient conversion of coproheme into heme *b*. This is indicated by the short and steep increase in absorbance, observed upon the addition of hydrogen peroxide as compared to the moderate and elongated elevation of the absorbance noticed during the titration with sodium chlorite.

#### 4.5.2 Variants, investigating the role of tyrosine 183

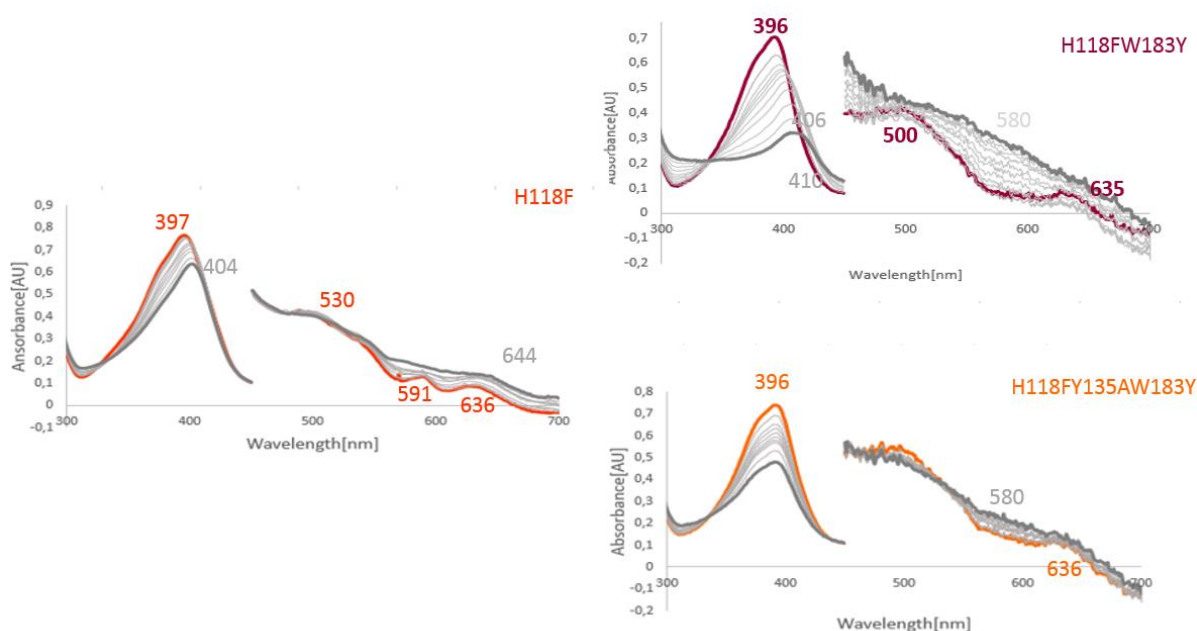


**Figure 23: UV-vis absorption spectra of H118F (red) and H118FW183Y (purple) and H118FY135AW183Y (orange).** The coloured spectra delineate the spectral properties of the coproheme-bound form of each variant, in the absence of the alternative substrate sodium chlorite.. A spectral transition can be followed as sodium chlorite is added in 2  $\mu$ M steps, resulting in the terminal, grey spectrum. The spectrum was enlarged by a factor of 5 from 450 nm for a detailed representation of the visible region.

H118F, upon sodium chlorite titration, exhibits a Soret maximum of 397 nm, which stepwisely shifts towards longer wavelengths to 404 nm. In the visible range, the CT band shifts from 636 nm to 644 nm. The maxima at 591 nm, recorded for the coproheme-bound form of H118F, disappears with increasing sodium chlorite concentration. Interestingly, the maximum at 530 nm is not affected during sodium chlorite titration.

The spectrum for H118FW183Y displays a maximum at 396 nm for the holo-variant. This maximum migrates to 410 nm as substrate addition progresses. The maxima at 500 nm and 635 nm diminish, while a characteristic, peak-like structure arises at 580 nm.



The triple variant, H118FY135AW183Y, shows an absorption maximum at 396 nm. The addition of substrate does not promote any shift in the absorption maximum but a decrease in absorption can be observed. The Q<sub>β</sub>-band at 491 nm disappears to the same extent as the CT band at 636 nm, while a small maxima at 580 nm appears.

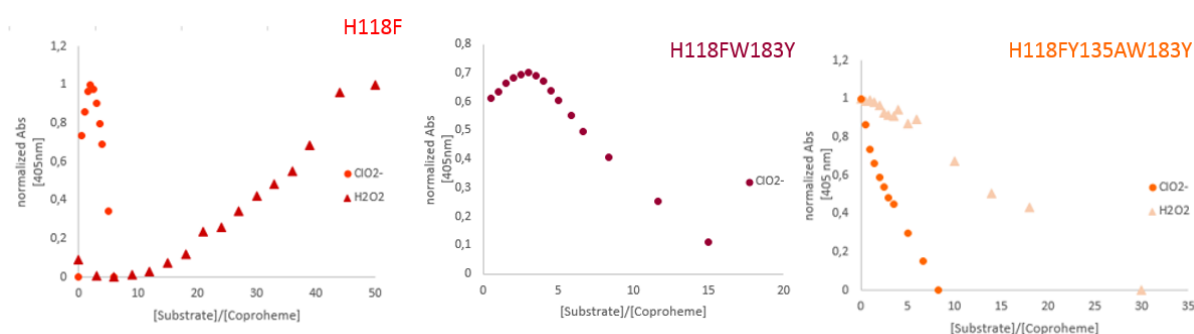


**Figure 24: Comparison of the substrates hydrogen peroxide and sodium chlorite for variants H118F, H118FW183Y and H118FY135AW183Y.** The circles represent the the ratio [sodium chlorite/coproheme] plotted against the normalized absorbance at 405 nm. The tringles delineate the ratio [hydrogen peroxide/coproheme] plotted against the normalized absorbance at 405 nm.

Figure 25 exhibits that the curve for the alternative substrate sodium chlorite displays a shorter and steeper slope compared to the natural substrate hydrogen peroxide. This indicated that the H118F variant converts coproheme into heme *b* more efficiently by the addition of sodium chlorite.

For the triple mutant, H118FY135AW183Y, a decrease in absorbance at 405 nm was observed for both of the substrates, indicating that the insertion of mutation led to the inability to convert coproheme into heme *b*.

#### 4.6 Pre-steady state kinetics

With the help of stopped-flow spectroscopy, the kinetic parameters of the variants have been examined. At first, the spectral behaviour of the variants was recorded using photodiode-array detector. Based on the obtained spectral information, a wavelength was defined at which the course of the reaction was followed over time.

#### 4.6.1 Tyrosine swap variants

Figure 26 depicts stopped-flow results of variant W183Y. Figure 23A provides information about the spectral transition, induced through the addition of hydrogen peroxide. The initial Soret maximum of 400 nm shifts to 412 nm. The maxima in the visible region at 504 nm and 630 nm alter with increasing hydrogen peroxide concentration, resulting in a maximum at 550 nm. The inset shows an exemplary time trace recorded at 393 nm for the W183Y variant. The course of the time trace indicates the appearance of a biphasic reaction which is completed after 3 s. To determine the apparent Compound I formation rate constants, each phase was single exponentially fitted to obtain the respective  $k_{obs}$  values. Figure 23B visualizes the correlation between  $k_{obs}$  and the substrate concentration. The linear slope indicates the concentration dependency of the performed reaction. W183Y revealed rate constants of  $6.27 \times 10^4 \text{ M}^{-1}\text{s}^{-1}$  for the first phase and  $3.97 \times 10^4 \text{ M}^{-1}\text{s}^{-1}$  for the second phase.

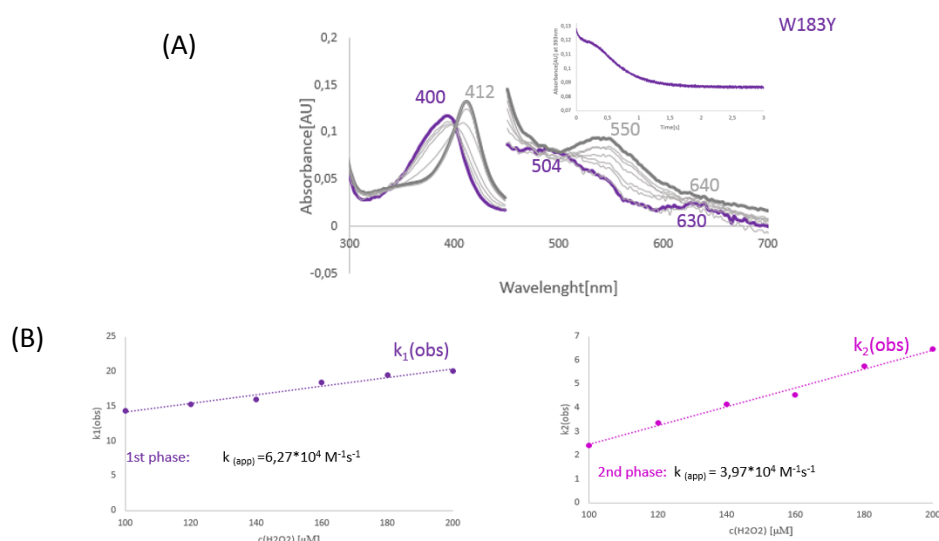


**Figure 25. Pre-steady state data obtained from W183Y variant.** (A) Provides information about the spectral transition induced by the stepwise addition of 20 μM hydrogen peroxide to 10 μM CdChdC admixed with 4 μM coproheme. The inset depicts an exemplary representation of a time trace of 10 μM CdChdC admixed with 4 μM coproheme and 120 μM hydrogen peroxide, recorded at 393 nm. (B) Visualizes the obtained  $k_{obs}$  values, plotted against the applied hydrogen peroxide concentrations (100 μM - 200 μM) for the first phase of the reaction as well as the second. Furthermore, the calculated apparent rate constants for both phases are presented in (B).

The W183YY135W variants spectral behaviour is displayed in figure 27, revealing the transit of the Soret maximum from 399 nm to 405 nm as well as the conversion of the maxima at 500 nm and 630 nm into a single maximum at 540 nm. The inset tracks the change in absorbance

with time at 393 nm for the double mutant W183YY135W. Comparing the time traces of W183Y and W183YY135W obvious differences can be spotted. The initial phase of the W183Y resembles a curve-like structure whereas W183YY135W revealed a linear slope as its initial phase. The second phase of W183Y appears to follow the course of an exponential function whilst W183YY135W exhibits a logarithmic trend. The calculated apparent rate constants were determined to be  $6.07 \times 10^4 \text{ M}^{-1}\text{s}^{-1}$  for the first phase and  $2.56 \times 10^4 \text{ M}^{-1}\text{s}^{-1}$  for the second phase. Both rate constants lie in the same magnitude as for the W183Y variant.

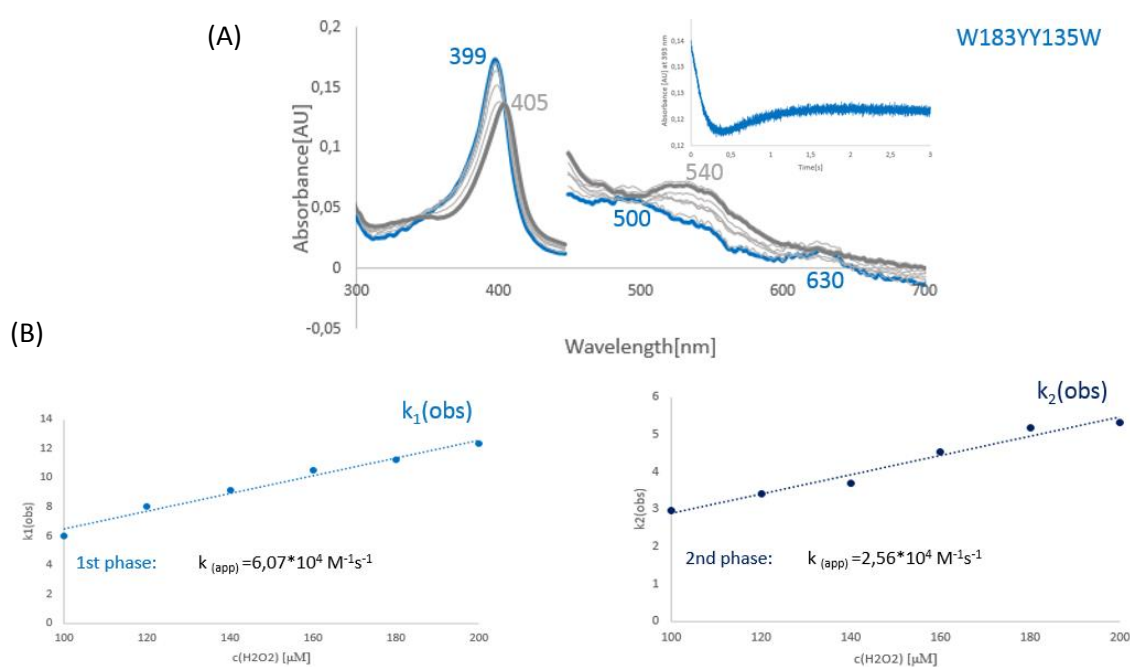


**Figure 26: Pre-steady state data obtained from W183YY135W variant.** (A) provides information about the spectral transition induced by the stepwise addition of 20 μM hydrogen peroxide to 10 μM CdChdC admixed with 4 μM coproheme. The inset depicts an exemplary representation of a time trace of 10 μM CdChdC admixed with 4 μM coproheme and 120 μM hydrogen peroxide, recorded at 393 nm. (B) Visualizes the obtained  $k_{\text{obs}}$  values, plotted against the applied hydrogen peroxide concentrations (100 μM - 200 μM) for the first phase of the reaction as well as the second. Furthermore, the calculated apparent rate constants for both phases are presented in (B).

Stopped-flow spectroscopy revealed a spectral transition for the W183YY135A variant, presented in figure 28, from 397 nm to 405 nm induced by the addition of hydrogen peroxide. Similar to the W183YY135A visible region, the W183YY135A revealed the passage of two maxima at 493 nm and 640 nm respectively into a single maxima at 580 nm. The inset depicts an example of a time trace recorded for the W183YY135A variant, suggesting the appearance of a biphasic reaction taking place. The course of the time trace in figure 25A, for the

W183YY135A has a very similar shape as the time trace for the W183YY135W variant. The respective apparent rate constant were figured out to be  $6.46 \times 10^4 \text{ M}^{-1}\text{s}^{-1}$  for the initial phase of the reaction and  $1.94 \times 10^3 \text{ M}^{-1}\text{s}^{-1}$  for the latter.

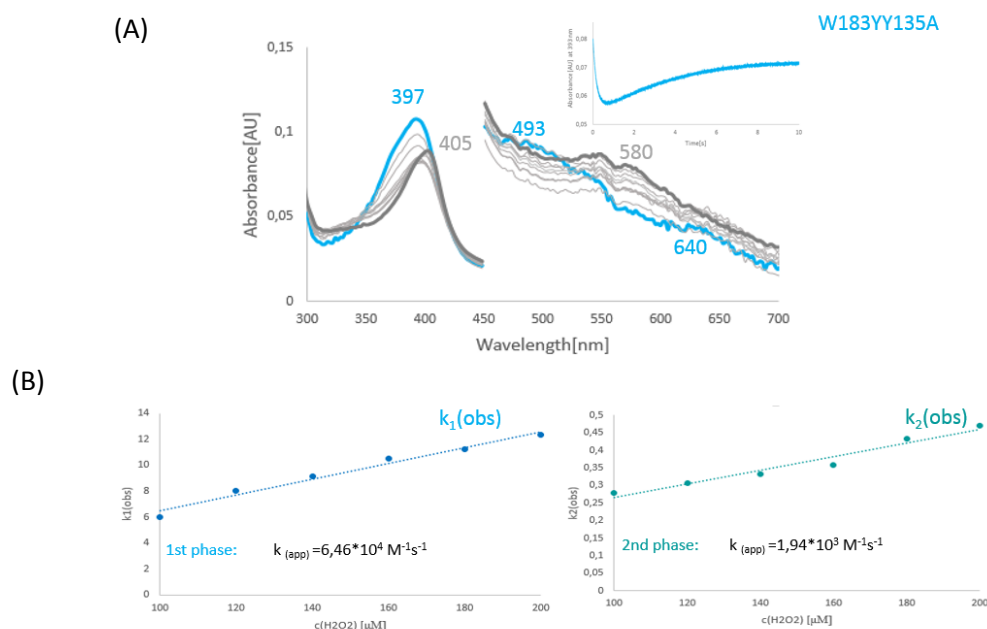


**Figure 27: Pre-steady state data obtained from W183YY135A variant.** (A) Provides information about the spectral transition induced by the stepwise addition of 20 μM hydrogen peroxide to 10 μM CdChdC admixed with 4 μM coproheme. The inset depicts an exemplary representation of a time trace of 10 μM CdChdC admixed with 4 μM coproheme and 120 μM hydrogen peroxide, recorded at 393 nm. (B) Visualizes the obtained  $k_{\text{obs}}$  values, plotted against the applied hydrogen peroxide concentrations (100 μM - 200 μM) for the first phase of the reaction as well as the second. Furthermore, the calculated apparent rate constants for both phases are presented in (B).

**Table 14: Determined apparent rate constants** of the WT and the variants W183Y, W183YY13W and W183YY135A.

	$k1(\text{app}) [\text{M}^{-1} \text{s}^{-1}]$	$k2(\text{app}) [\text{M}^{-1} \text{s}^{-1}]$
WT	$4.90 \times 10^4$	
W183Y	$6.27 \times 10^4$	$3.97 \times 10^4$
W183YY135W	$6.07 \times 10^4$	$2.56 \times 10^4$
W183YY135A	$6.46 \times 10^4$	$1.94 \times 10^3$

Table 14 summarizes the obtained apparent rate constants of the examined variants and the WT. The observed apparent rate constants range in the same magnitude as the wild-type. This

observation is visualized by a web diagram (Figure 26), which indicates that all apparent rate constants of the first phase arrange at almost the same distance relative to zero. The rate constants for an eventual second phase of the reaction lie within the same magnitude for the W183Y and The W183YY135W variant. The magnitude of these two rate constants range in the magnitude of the first phase rate constants. The second phase of the W183YY135A seem to appear one magnitude slower than in the variants W183Y and W183YY135W.

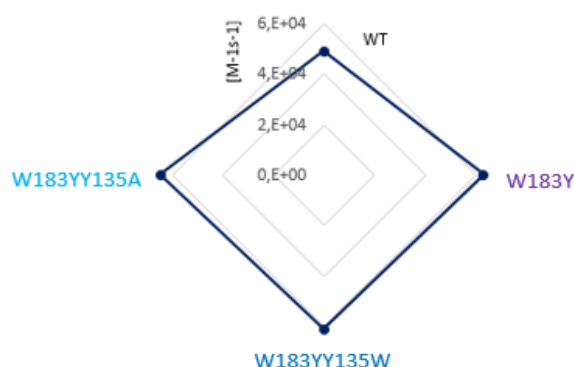


**Figure 28: Comparison of the determined apparent rate constants** of the WT and the variants W183Y, W183YY135W and W183YY135A.

#### 4.7 Steady-state kinetics

Steady state kinetic parameter are determined to investigate the behaviour of the WT enzyme and its variants in the beginning of a reaction in a steady state. Steady state kinetics are used to obtain information on  $K_M$ ,  $k_{cat}$  and the specificity constant ( $k_{cat}/K_M$ ).

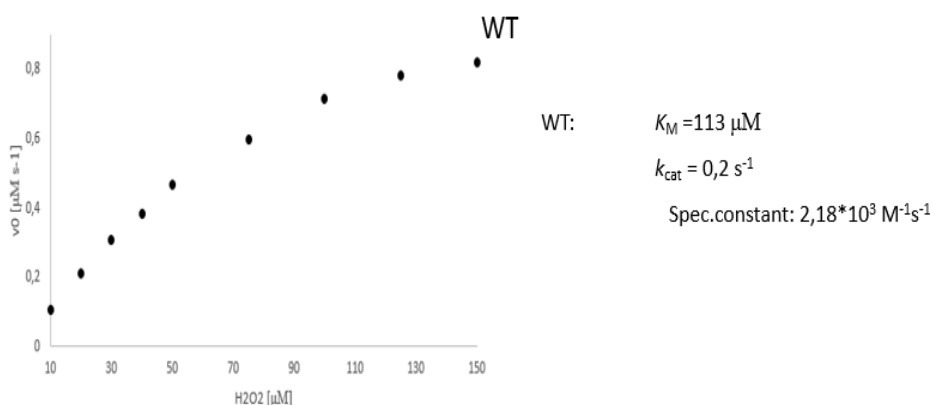


**Figure 29: Steady-state kinetics of the CdChdC-WT.** (A) The obtained initial velocity plotted against the applied hydrogen peroxide concentration (10  $\mu\text{M}$  - 150  $\mu\text{M}$ ), which is added to 10  $\mu\text{M}$  CdChdC WT and 5  $\mu\text{M}$  coproheme, to obtain steady-state kinetic parameter, which are presented in (B).

In figure 30 steady state results for the WT are displayed. To obtain steady state kinetic parameters the substrate concentration is first plotted against the initial velocity, which was obtained by stopped-flow spectroscopic measurement. The data was then linearized using a Hanes plot. With the help of the Hanes plot the kinetic parameters were obtained. The WT revealed a  $K_M$ -value of 113  $\mu\text{M}$ , a  $k_{\text{cat}}$  value of  $0.2 \text{ s}^{-1}$  and a specificity constant of  $2.18 \times 10^3 \text{ M}^{-1} \text{ s}^{-1}$ .

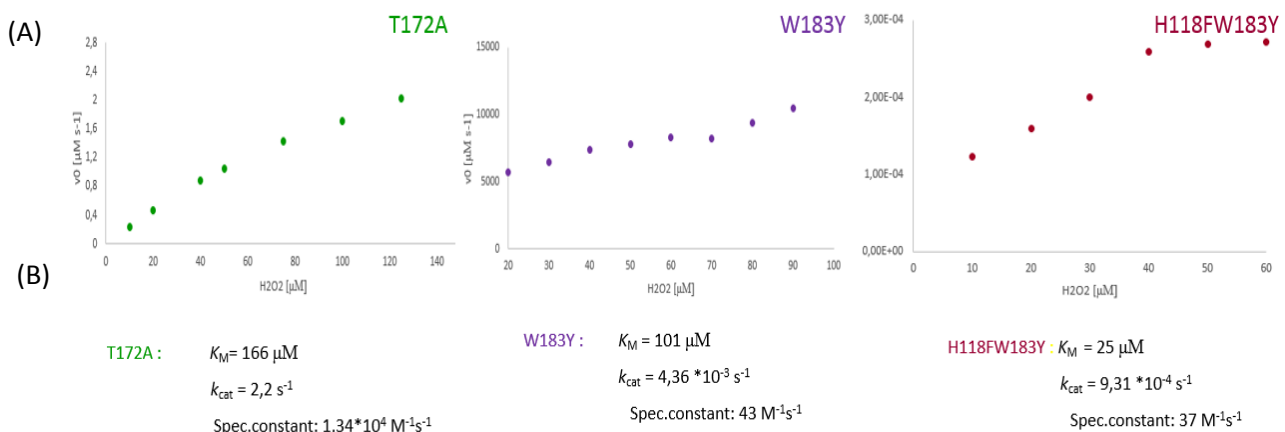


**Figure 30: Steady-state kinetics of T172A (green), W183Y (violet) and H118FW183Y (purple).** (A) The obtained initial velocities plotted against the applied hydrogen peroxide concentration (10  $\mu\text{M}$  - 150  $\mu\text{M}$ ), which is added to 10  $\mu\text{M}$  CdChdC WT and 5  $\mu\text{M}$  coproheme, to obtain steady-state kinetic parameters, which are presented in (B).

Figure 31 presents the results for the T172A, W183Y and H11FW183Y variants obtained through steady state observations. The T172A steady state kinetic parameters were calculated to be 166  $\mu\text{M}$  for the  $K_M$ -Value, being slightly higher than the  $K_M$ -Value for the WT. The W183Y revealed a  $k_{\text{cat}}$  of  $2.2 \text{ s}^{-1}$  and a specificity constant of  $1.34 \times 10^4 \text{ M}^{-1} \text{ s}^{-1}$ . The  $k_{\text{cat}}$  value as well as the specificity constant of the W183Y show slightly elevated values compared to the values of the WT.

The W183Y in contrast to the T172A revealed lower values for its enzymatic behaviour in steady state conditions as the WT. The  $K_M$  value was figured out to be 101  $\mu\text{M}$  and the  $k_{\text{cat}}$  was determined to be  $4.36 \times 10^{-3} \text{ s}^{-1}$ , which is lower by two orders of magnitude compared to the WT. The same difference of magnitude can also be observed by the comparison of the specificity constants of the W183Y and the WT with values of  $43 \text{ M}^{-1} \text{ s}^{-1}$  and  $1.34 \times 10^4 \text{ M}^{-1} \text{ s}^{-1}$  respectively.

For the H118FW183Y the  $K_M$  value was considered to be 25  $\mu\text{M}$  and therefore being one magnitude lower than the  $K_M$  of the WT. A  $k_{\text{cat}}$  of  $9.31 \times 10^{-4} \text{ s}^{-1}$  was calculated for the H118FW183Y variant.

## 4.8 Electronic circular dichroism

### 4.8.1 Far UV electronic circular dichroism (ECD)

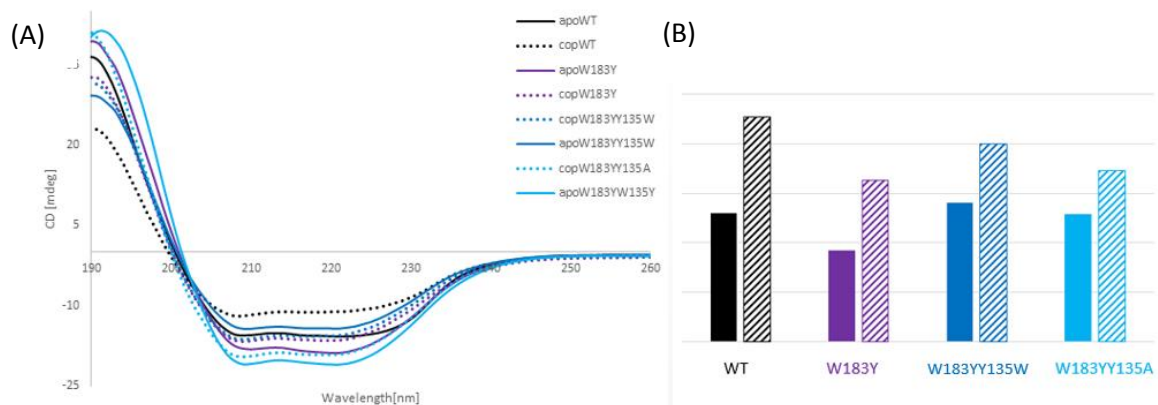


**Figure 31: ECD spectra in the far UV-region. (A)** The full lines representing the apo-form of the WT (black), W183Y (violet), W183YY135W (blue) and W183YY135A. The dotted lines delineate the holo-form of the respective variants of CdChdC. **(B)** Ellipticity ratio 208nm/222 nm of the apo (plain bars) and the holo-variants (dashed bars).

Far UV ECD aims to provide information on the secondary structure elements of the examined variants. Secondary structural motifs can be associated to distinct characteristics depicted in the far-UV ECD spectrum. Figure 32 reveals the ECD spectrum of the WT and its respective variants. The apoWT (black line) spectrum indicates a maximum at 192 nm as well as two minima at 209 and 222 nm respectively, which are characteristic for the predominance of  $\alpha$ -helical secondary structures. Comparing the spectra of the apo-variants to WT, all of them exhibit a WT-like secondary structure.

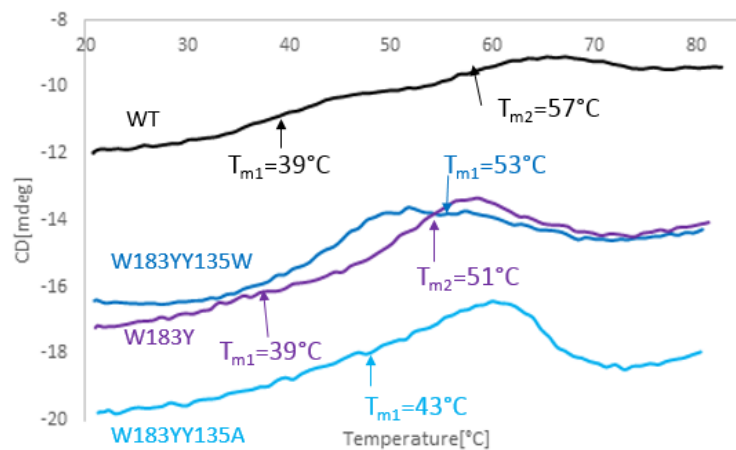
The dashed-lines in the spectra of figure refer to the holo-form of the WT and its variants. Coproheme binding induces a conformational change in the WT, which is expressed in an obvious alteration of the ECD spectrum. Minor deviations between the apo- and the holo-spectra of the variants W183Y, W183YY135W and W183YY135A are also observed.

Figure 32B illustrates the ellipticity ratio of 208 nm and 222 nm of the proteins. The dashed bars refer to the apo-form and the plain bars to the corresponding holo-form. A decrease in the ellipticity ratio is a clear indication of the induction of a conformational change upon coproheme binding.

#### 4.8.2 Thermostability

Besides information on secondary structure conformation, ECD can be used to investigate the behaviour of the WT and variants under varying thermal conditions. Thermostability observations were done in the near UV region to investigate the influence of a temperature gradient on the unfolding and refolding properties. Furthermore, the impact of an elevated temperature on secondary structure conformation was examined.

##### Near UV region



**Figure 32:** Unfolding curves of WT (black), W183Y (violet), W183YY135W (blue) and W183YY135A (light-blue). Recorded at 393 nm and the corresponding melting temperatures of the respective variants.

Thermal unfolding characteristics of the WT and variants are summarized in figure 33, outlining the recorded temperature curves. The WT and W183Y temperature curves reveal two transitions representing melting points whereas W183YY135A and W183YY135W seem to have one single melting point. The  $T_{m1}$  value of the WT and the W183Y mutant is associated with the heme release event due to the thermally induced rearrangement of the active site



architecture. The  $T_{m2}$  values correspond to the unfolding of the protein's secondary structural elements. A single  $T_m$ -value, as obtained for W183YY135A and W183YY135W, outline a simultaneous heme release and denaturation event.

The temperature of 39°C, obviously marks the point at which the active site is destroyed to that certain extent, which makes the protein incapable of bearing the coproheme.

The comparison of the melting points delineates that the W183YY135A shows the lowest melting point of 43°C, indicating the least stability and the WT with a melting point of 57°C, the highest.

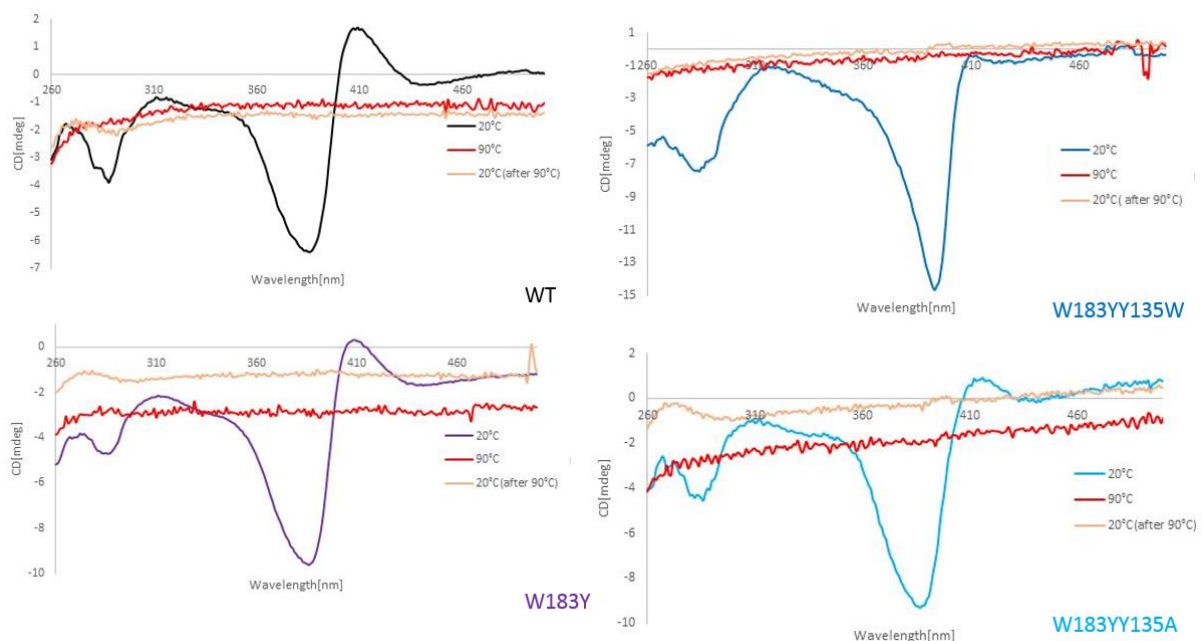


**Figure 33: Unfolding thermographs of the WT (black), W183Y (violet), W183YY135W (blue) and W183YY135A (light-blue).** The spectrum, in the respective colour for each variant, illustrates the spectral properties of the holo-form of each variant at 20°C. The red spectra depict the enzymatic behaviour of each variant at 90°C and the orange spectra points out, the spectral properties of each variant after the re-establishment of 20°C.

Figure 34 outlines the behaviour of the coproheme-bound form of the proteins under varying thermal conditions. The spectra provide information on the spectral properties of the protein at 20°C (coloured spectra). All spectra show a distinct maximum at 386 nm, corresponds to the absorption maximum of the coproheme in its bound form. With an increase of temperature to 90°C (red spectrum) the peak diminishes completely, indicating the release of the substrate due to thermally contingent unfolding. The orange spectra point out the spectral behaviour of the proteins after the reestablishment of 20°C. The close resemblance of the red

and the orange spectrum suggest, that the elevation of temperature induces an irreversible unfolding of the proteins.

#### Far UV region

Thermostability studies, performed in the far UV region underlined the results obtained by near UV-vis-ECD. The spectra for the respective variants demonstrate the characteristic minima (209 nm and 222 nm) and a maximum (192 nm) associated with an  $\alpha$ -helical secondary structure. Upon heating these characteristic features vanish, indicating an unfolding process. After restoration of the initial temperature of 20°C, the characteristics traits remain disappeared, implying an irreversible unfolding process.

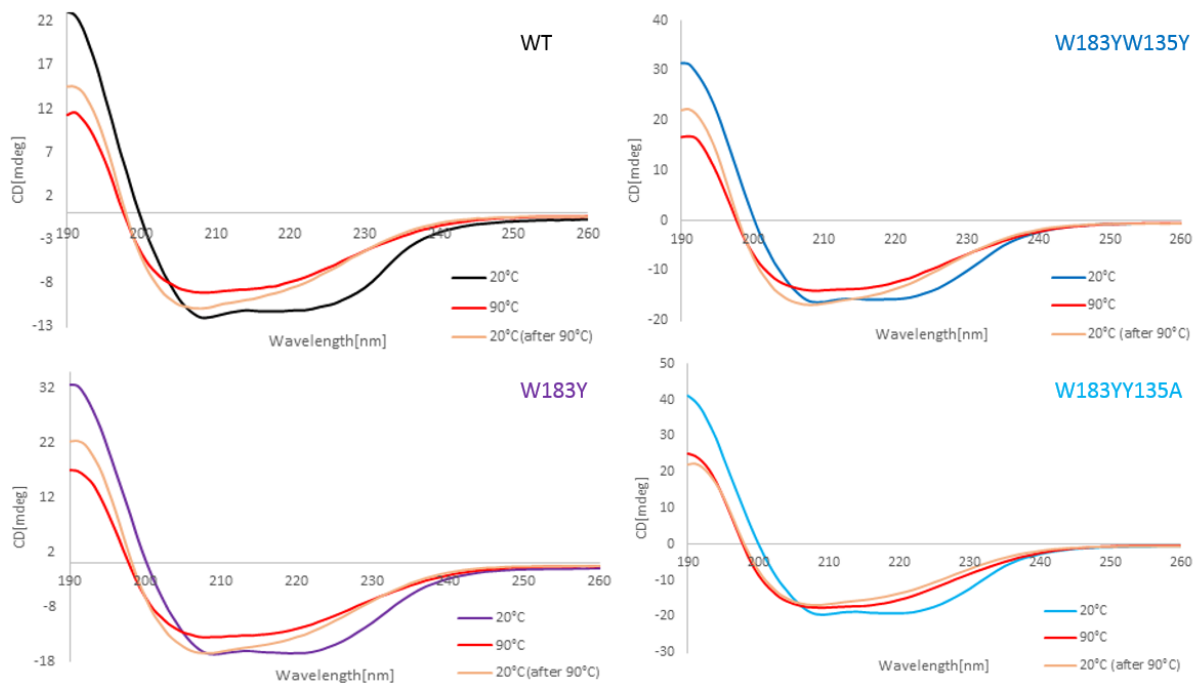
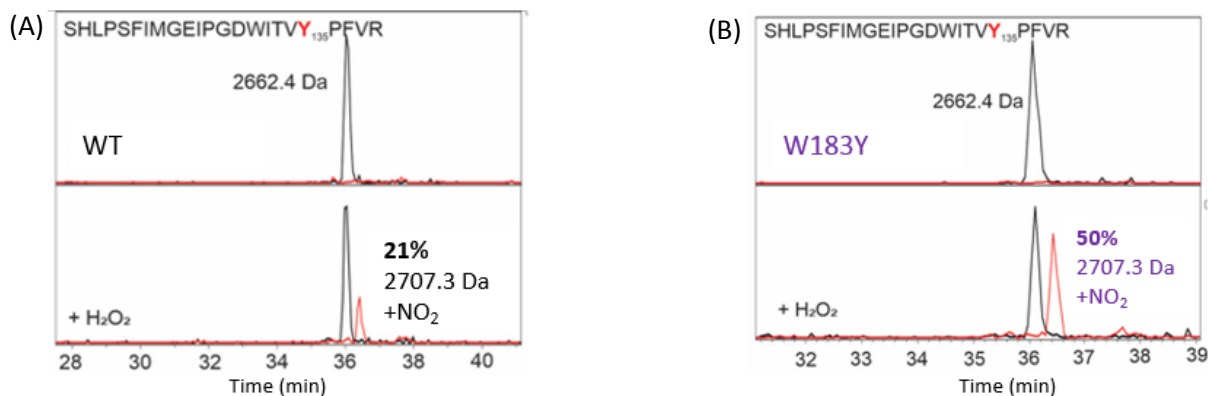


Figure 34: ECD thermographs in the far UV region of WT (black), W183Y (violett), W183YY135W (blue) and W183YY135A (light-blue). The spectrum, in the respective colour for each variants, illustrates the spectral properties of the holo-form of each variant at 20°C. The red spectra depict the enzymatic behaviour of each variant at 90°C and the orange spectra points out, the spectral properties of each variant after the re-establishment of 20°C.

## 4.9 MNP spin trapping

To investigate and highlight the radical formation potential of the native tyrosine 135 and the artificial tyrosine 183, spin trapping experiment have been conducted. Figure 36A provides information on the degree of nitrosylation of the tyrosine 135 from the CdChdC-WT. In the top spectrum, which was recorded in the absence of hydrogen peroxide, a single peak can be spotted. This peak refers to a molecular mass of 2662 Da, which correlates to the size of the peptide in which includes the native tyrosine. The bottom spectrum in figure 36A resembles the behaviour of the same peptide after the addition of hydrogen peroxide. With the addition of hydrogen peroxide, a second red peak appears, which refers to a molecular mass of 2707.3 Da. This increase in molecular mass by 44.98 Da indicates the linkage of 2-methyl-2-nitrosopropane to the radical tyrosine. W183Y revealed similar results (shown in figure 33B) for the spin-trapping experiment. Without hydrogen peroxide, only one peak at 2664.4 Da was detected whilst the addition of substrate induced the growth of a second peak shifted by 44.98 Da. The only difference, which can be spotted, lies in the detected degree of nitrosylation. The tyrosine 135 in the W183Y variant was twice as much nitrosylated as the tyrosine 135 of the WT.



**Figure 35: MS-analysis spectra of the WT (A) and W183Y (B), investigating the nitrosylation of tyrosine 135.** The top spectra represent the peptide in the absence of hydrogen peroxide, whereas the bottom spectra highlight the peptide after the addition of hydrogen peroxide.

Figure 37 depicts MNP spin-trapping results of the WT (A), W183Y (B) and W183YY135A (C), focusing on the artificial tyrosine on position 183. For the WT, lacking the artificial tyrosine 183, two identical spectra were obtained, with and without the addition of hydrogen peroxide,

indicating, that no nitrosylation occurred due to the lack of a tyrosine residue on the respective position. In the W183Y variant in contrast, the incorporated tyrosine 183 was affected by a nitrosylation. This nitrosylation is indicated by the appearance a second, minor peak upon the addition of hydrogen peroxide offset to the prominent maximum at 36 min.

Figure 37C illustrates nitrosylation results for the tyrosine 183 of W183YY135A. The appearance of the second, red maximum indicates that the tyrosine 183 is modified upon the addition of hydrogen peroxide. The degree of nitrosylation in both, the W183Y and W183YY135A variant, range in the same range with 11% and 15%, respectively.

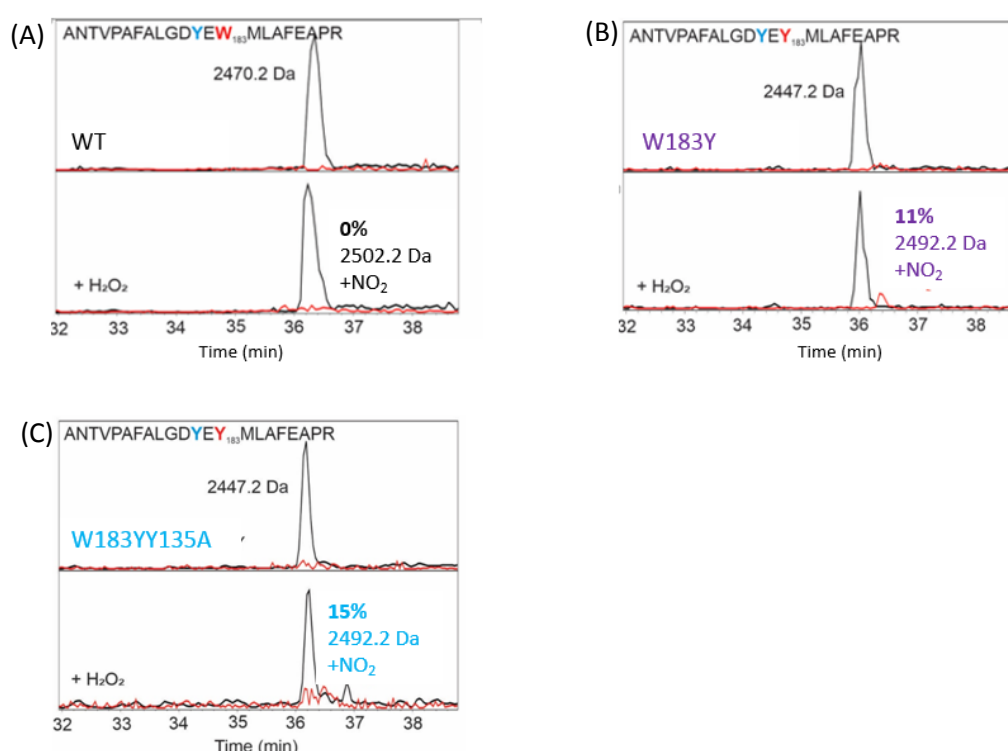


**Figure 36: MS-analysis spectra of the WT (A) and W183Y (B) and W183YY135A(C), investigating the nitrosylation of tyrosine 183Y.** The top spectra represent the peptide in the absence of hydrogen peroxide, whereas the bottom spectra highlight the peaks of the peptide after the addition of hydrogen peroxide.

#### 4.10 Matrix assisted laser desorption/ionization

MALDI analysis was performed to track the conversion process of coproheme into heme *b* of the distinct variants. Furthermore, the method is used to qualitatively identify the established heme species of each variant. The substrate coproheme is identified by a maximum in the MS spectrum by a mass-charge ratio of 708 (corresponding to 708 Da). Upon addition of hydrogen peroxide the maxima at 708 m/z decreases and a peak at 662 m/z appears. The peak at 662

$m/z$  refers to the presence of the reaction intermediate MMD. The peak at 662  $m/z$  diminished with the further addition of hydrogen peroxide while a peak at 617  $m/z$  becomes visible. This peak at 617  $m/z$  indicates the presence of the heme *b*.

#### 4.10.1 Tyrosine swap variants

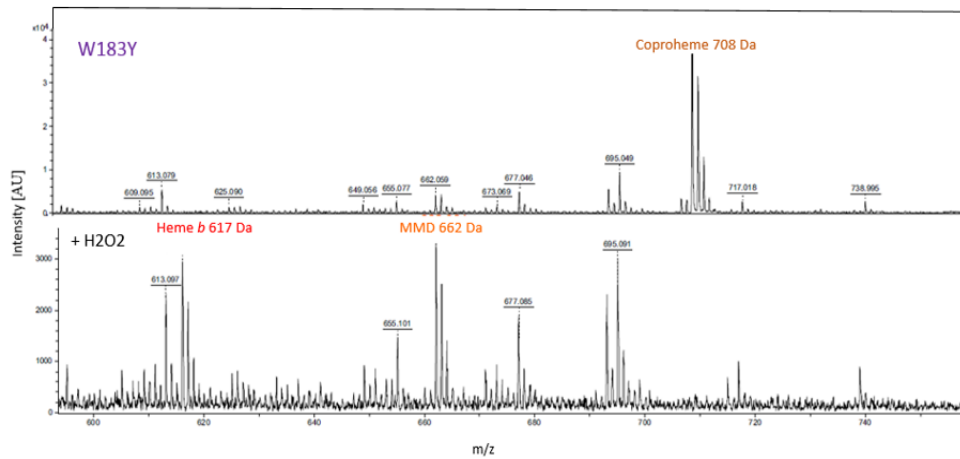


**Figure 37: MS-spectra of W183Y variant.** Top spectrum highlights iron species present in the absence of hydrogen peroxide, whereas the bottom spectra reveals iron species produced upon the addition of hydrogen peroxide.

MALDI analysis revealed the capacity of the W183Y variant (Figure 38), as the peak at 708  $m/z$  disappeared upon the addition of hydrogen peroxide. In exchange for the disappearance of the 708  $m/z$  peak, a peak at 662  $m/z$  and a peak at 616  $m/z$  emerge. As already mentioned above the 662  $m/z$  peak refers to the presence of the intermediate MMD, which is converted into heme *b*. The presence of a heme *b* species is indicated by the maximum at 616  $m/z$ .

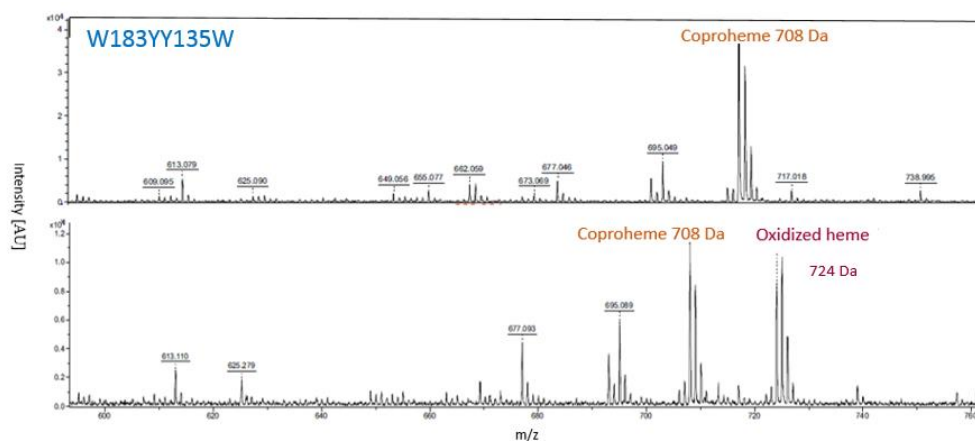


**Figure 38: MS-spectra of W183YY135W variant.** Top spectrum highlights iron species present in the absence of hydrogen peroxide, whereas the bottom spectra reveals iron species produced upon the addition of hydrogen peroxide.

The W183YY135W variant (Figure 39), in contrast revealed its inability to perform the conversion of coproheme into heme *b*. Instead of the desired maximum at 616 m/z the variant exhibits a peak at 724 m/z. The initial maximum at 708 m/z of coproheme shifts to the left by a m/z value of 16 to 724 m/z. The increase in the m/z ratio by 16 is a strong indication for the covalent linkage of oxygen to the coproheme, resulting in the oxidized heme species heme *d*. Interestingly, the signal intensity of the coproheme peak remains unaltered, indicating that the substrate mostly stays unaffected and only a small moiety of it is converted into oxidized heme.

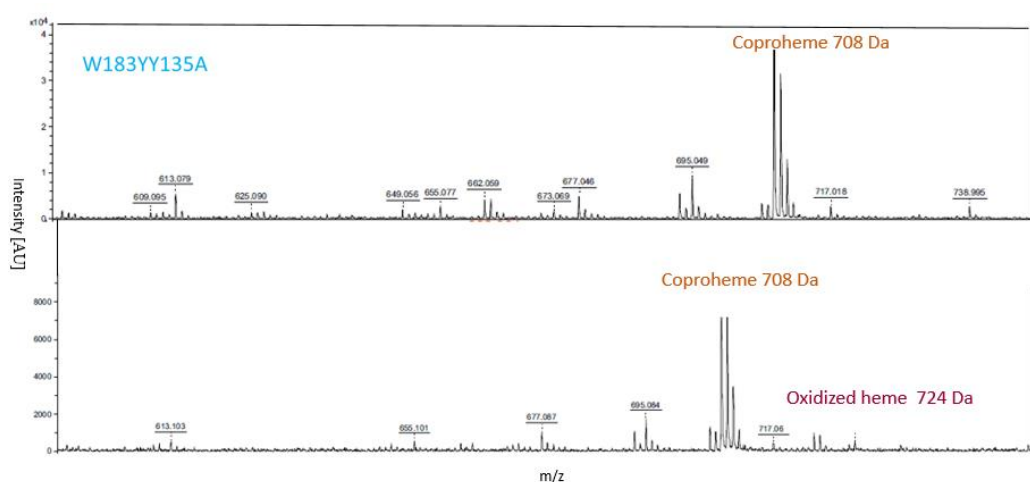


**Figure 39: MS-spectra of W183YY135A variant.** Top spectrum highlights iron species present in the absence of hydrogen peroxide, whereas the bottom spectra reveals iron species produced upon the addition of hydrogen peroxide.

The W183YY135A (Figure 40) variant exhibits a similar behaviour upon hydrogen peroxide addition as the W183YY135W variant. Instead of converting the substrate coproheme into the final product heme *b*, coproheme gets oxidized into heme *d*. This conversion into an oxidized heme species is indicated by a tiny maximum at 724 m/z.

#### 4.10.2 Variants, investigating the role of tyrosine 183

The spectra of the H118F (Figure 41A) variant depicts the MMD-formation potential of the H118F variant as a prominent peak appears at a mass- charge ratio of 662 upon the addition of hydrogen peroxide. A similar behaviour can be observed for the H118FW183Y (Figure 41B) variant. Only a difference in the intensity of the signal stands out. The H118FY135AW183Y

variant (data not shown) exhibited its inability to convert coproheme into heme *b*, as only a maximum at 724 m/z appears as hydrogen peroxide was added.

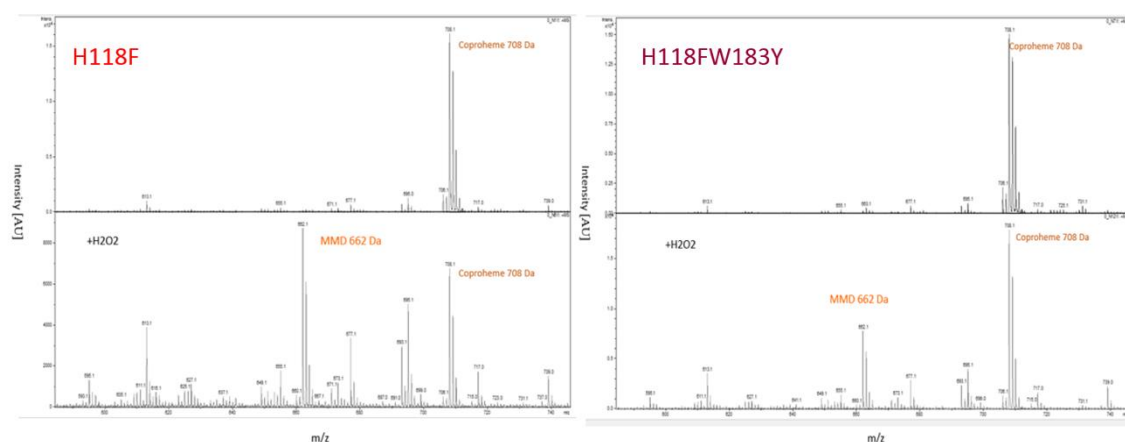


**Figure 40: MS-spectra of H118F(A) and H118FW183Y (B).** Top spectra highlight iron species present in the absence of hydrogen peroxide, whereas the bottom spectra reveals iron species produced upon the addition of hydrogen peroxide.

As expected, the T172AW183Y (Figure 42A) variant, converted coproheme via MMD into heme *b* in a WT-like manner. This WT-like behaviour is indicated by the presence of a peak at 662 m/z and 616 m/z respectively. In contrast, the T172AY135AW183Y triple variant revealed a deviant behaviour than the WT. Only a minor maximum at 724 m/z can be spotted in the spectrum of T172AY135AW183Y (Figure 42B), indicating the covalent linkage of oxygen to the substrate coproheme upon the addition of hydrogen peroxide.

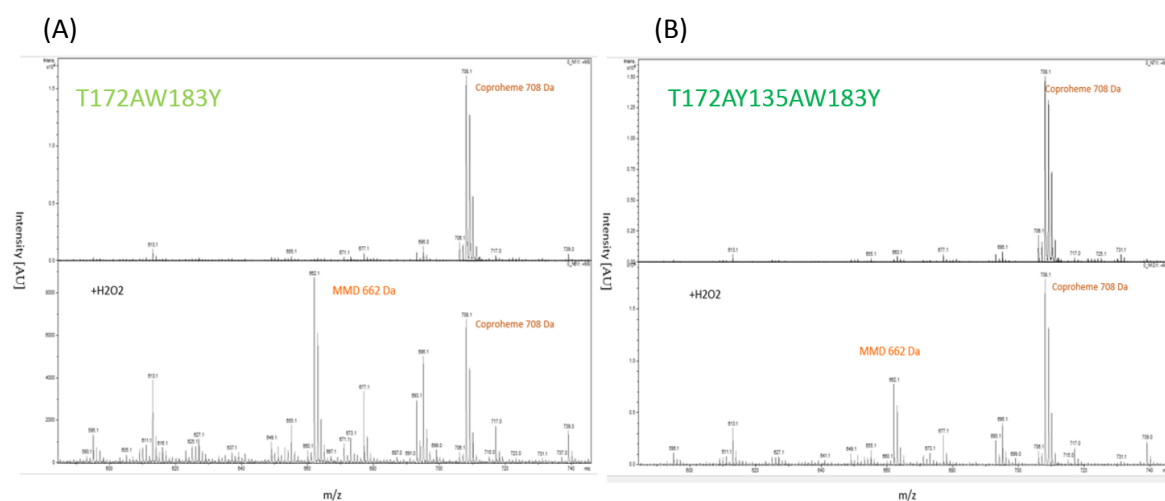


**Figure 41 : (A) MS-spectra of T172AW183Y (A) and T172AY135AW183Y (B).** Top spectrum highlights iron species present in the absence of hydrogen peroxide, whereas the bottom spectra reveals iron species produced upon the addition of hydrogen peroxide.

## 5 Discussion

This master thesis aimed to study the mechanistic behaviour of various variants of corynebacterial coproheme decarboxylase from *Corynebacterium diphtheriae*. For this purpose, ChdC variants have been designed and established. Prior to recombinant protein production, a test expression was conducted to probe the functionality of the expression system. A comparison of the induced and non-induced lysate of an expression system with the help of a SDS-page (Figure 15) revealed, that all expression systems are perfectly functional. The target proteins were then recombinantly expressed in *E. coli* Tuner (DE3) cells and purified by metal chelate affinity chromatography, yielding reasonable amounts of the desired proteins in the range between 20 mg and 55 mg per 750 mL culture (Table 13). A slightly reduced yield for variants T172AY135AW183Y and H118FY135AW183Y might be led back to the insertion of multiple mutations, which influences the expressability and the stability of the variants. A decreased yield of the H118F variants might correlate with the importance of the exchanged amino acid, as the histidine in the WT-ChdC is used as distal base to promote the formation of compound I (24). As a quality control, regarding the integrity and the purity of the variants, a HPLC-SEC MALS analysis was implemented. All variants exhibited a retention time, characterized by a peak at 16 min for the apo-enzyme as well as for the coproheme-bound form of the enzyme in their chromatogram (Figure 16). In some chromatograms, like for the WT and the variants T172AY135AW183Y, T172AY135A, H118FW183Y, H118FY135AW183Y and W183YY135A, a second, upstream peak occurs. These peaks can be traced back to the presence of impurities in the sample, which are most likely ChdC aggregates (10-mers instead of pentamers). For the removal of these impurities, a second purification run by size exclusion chromatography can be performed.

With the completion of the quality control of the variants, this work progressed with the characterization of the CdChdC-tyrosine swap variants in terms of their spectral properties and their substrate binding ability (Figure 17). The characteristic maxima of free coproheme in solution at 390 nm, 612 nm, 530 nm and 466 nm, manifestly alter in variants W183Y and W183YY135A, as binding of the coproheme to the active site takes place. Maxima at 396 nm, 640 nm, 530 nm and 490 nm characterize holoW183Y, whereas holoW183YY135A exhibits maxima at 399 nm, 509 nm and 648 nm. An alteration in the absorption maxima signalizes a modification of the spin state of the iron coordinated in the coproheme. Upon substrate



binding the spin state of the coproheme iron in W183Y and W183YY135A changes from five-coordinated high spin (5cHS) to a six-coordinated high-spin (6cHS) species in the holo-variants. For W183YY135W, only one maximum migrates, namely the maximum from 390 nm to 399nm. As the charge transfer band remain unaltered, coproheme binding does not effect five-coordinated low spin state of the coproheme iron. Regarding the binding capacity of the respective variants, it can be stated that variants W183Y and W183YY135A require a similar ratio of enzyme to substrate to obtain a fully occupied active site. In comparison, the W183YY135A variants, less efficiently binds coproheme as substrate to its active site. A reduced binding capacity might be connected to the nature of the inserted amino acid, as tyrosine and tryptophan vary significantly in the nature of their structure.

The decarboxylase activity of the variants has been investigated by a hydrogen peroxide titration followed by UV-vis spectroscopy *CdChdC*-WT, with its native decarboxylation activity (Figure 18), revealed a spectral transition upon the addition of hydrogen peroxide. The maxima of the holoWT migrate from 393 nm, 504nm and 643 nm to 406 nm and 602 nm with increasing hydrogen peroxide concentration. The diminishing of the CT-band at 643 nm, indicate the change of the spin-state from five-coordinated high spin to six-coordinated low spin. The faint of the CT-band is observed in all tyrosine swap mutants, W183Y, W183YY135W and W183YY135A respectively. The W183Y variant, carrying the native tyrosine 135 and an engineered tyrosine on position 183, revealed a spectral transition from 400 nm to 411 nm. The presence of the native tyrosine, indicates the ability of the W183Y variant to convert coproheme into heme *b* upon the addition of hydrogen peroxide. The decarboxylation ability of the W183Y variant is confirmed by MALDI-TOF analysis (Figure 38), revealing the presence of heme *b* as hydrogen peroxide is added.

A spectral transition from 399 nm to 406 nm in the W183YY135W variant and from 399 nm to 406 nm in the W183YY135A is observed with increasing concentration of hydrogen peroxide. By means of the results obtained through UV-vis spectroscopy, it could be speculated that a decarboxylation ability was promoted to variants W183YY135W and W183YY135A. The decarboxylation ability of the variants W183YY135W is disproven by MALDI-TOF analysis. For variants W183YY135W (Figure 39) and W183YY135A (Figure 40), oxidized heme or heme *d*, was the only heme species to be identified by MS-analysis. MALDI analysis therefore, delivered proof, that the incorporation of an engineered, artificial tyrosine at position 183 does not induce the establishment of a stereospecific reaction

intermediate MMD, although MNP-spin trapping results for W183YY135A (Figure 37C) highlighted the successful radical formation of the artificial tyrosine 183, as 2-methyl-2-nitrosopropane specifically links to radical species. The radical formation potential of the artificial tyrosine was confirmed by MNP-spin trapping results of W183Y (Figure 37B). The incorporation of a second reaction performing tyrosine into the active site of *CdChdC*, result in a deviating enzymatic behaviour of the W183Y compared to the WT, in terms of steady state kinetics. A  $K_M$  of 101  $\mu\text{M}$ , a  $k_{\text{cat}}$  of  $4.36 \times 10^{-3} \text{ s}^{-1}$  and a specificity constant of  $1.34 \times 10^4 \text{ M}^{-1} \text{ s}^{-1}$  characterize the W183Y (Figure 26) variant compared to the values of the *CdChdC*-WT, with a  $K_M$ -value of 113  $\mu\text{M}$ , a  $k_{\text{cat}}$  value of  $0.2 \text{ s}^{-1}$  and a specificity constant of  $2.18 \times 10^3 \text{ M}^{-1} \text{ s}^{-1}$ . The decrease of two magnitudes in terms of turnover number and substrate specificity are the foundations of the assumption that the incorporation of a second, reaction performing tyrosine enhances and optimizes the decarboxylation ability of coproheme decarboxylase. Interestingly, the determined apparent rate constant ( $k_{\text{app}}$ ) for the W183Y (Figure 31) and the WT (Figure 30) range in the same magnitude, namely  $6.27 \times 10^4 \text{ M}^{-1} \text{ s}^{-1}$  and  $429 \times 10^4 \text{ M}^{-1} \text{ s}^{-1}$  (24) respectively. As the W183Y variant and the WT resemble in their compound I formation behaviour, the addressed optimization of the decarboxylation processes might take place in the second phase of the reaction. Worth mentioning, might be the observation that an eventual decarboxylation activity of tyrosine 183 occurs in the presence of the native tyrosine 135 as the catalytic parameters in W183Y significantly change with the addition of a second reaction performing character but no catalytic activity was observed with the engineered tyrosine, only.

A comparison of the determined apparent rate constants of W183YY135W (Figure 27) and W183YY135A (Figure 28) to the WT, with  $6.07 \times 10^4 \text{ M}^{-1} \text{ s}^{-1}$  and  $6.46 \times 10^4 \text{ M}^{-1} \text{ s}^{-1}$  respectively, show no significant variance to the WT.

The triplet of histidine variants, namely H118F, H118FW183Y and H118FY135AW183Y should serve as a confirmation of the decarboxylation activity of the tyrosine 183. As already mentioned, the H118F variant is known to be sterically block the rotation of the MMD after the completion of the first decarboxylation (24). With the incorporation of the Y183, we hoped to rule out the blockage and repromote the heme *b* formation power to H118FW183Y. Unfortunately already hydrogen peroxide titration followed by UV-vis spectroscopy disproved these assumptions. The H118FW183Y (Figure 21) displayed similar spectral properties as the single mutant H118F, leading to the indication that conversion of coproheme to heme *b* also

terminates after the establishment of MMD. This indication was then confirmed by MALDI-analysis (Figure 41A), which detected the presence of MMD but not the desired heme *b*. For the H118FY135AW183Y (Figure 21), a decrease of the maxima at 392 nm was observed with increasing hydrogen peroxide concentration as well as a small maximum at 580 nm, which can be traced back to the presence of oxidized heme.

The histidine variants were also probed with the alternative two-electron donor sodium chlorite. Sodium chlorite titration followed by UV-vis spectroscopy (Figure 24), revealed the same spectral properties as with hydrogen peroxide leading to the conclusion that the change in substrate does not have an influence on the mechanistic behaviour of the investigated variants. A qualitative comparison (Figure 25), although, unveiled an increased efficiency in the conversion of coproheme into heme *b* with the alternative substrate sodium chlorite. An elevated efficiency towards sodium chlorite is dedicated to the lack in an initial deprotonation step required, when sodium chlorite is offered as alternative electron donor. The H118 has been identified to be involved in this initial deprotonation step (24). With sodium chlorite, this step is omitted and therefore the efficiency of variants H118F and H118FW183Y towards sodium chlorite seems to be increased. This is also underlined by the results obtained when examining the influence of the alternative substrate sodium chlorite on the tyrosine swap variants W183Y, W183YY135W and W183YY135A (Figures 22 and 23). The presence of a histidine 118 leads to an increased efficiency with the natural substrate hydrogen peroxide than with sodium chlorite.

As decarboxylation activity was not successfully promoted to tyrosine 183 in variants H118FW183Y and H118FW183Y, a series of threonine variants, namely T172A; T172AY135A; T172W183Y and T172AY135AW183Y, have been established. With the removal of the threonine 172 in variants T172AW183Y and T172AY135AW183Y, it was assumed to deplete the electron transfer route towards tyrosine 183 and therefore channel the charge transfer onto Y183 to successfully promote decarboxylation to the engineered tyrosine. Furthermore, the role of the threonine in the overall decarboxylation process was investigated with variants T172 and T172AY135A.

The absorption maxima of the coproheme-bound T172A (Figure 19) lie at 399 nm, 504 nm and 640 nm. Hydrogen peroxide induces the shift of the maximum to 410 nm, whereas the local maxima in the visible region remain unaltered. The presence of the CT-band at 640 nm without

and with hydrogen peroxide indicate that the five-coordinated high-spin state of the iron does not change with the addition of the substrate. The presence of the native tyrosine leads to the conclusion that the T172A variant is prone to convert coproheme into heme *b*. In contrast to the double mutant T172AY135A (Figure 19), lacking the native tyrosine. The holoT172AY135A, revealed maxima 394 nm, 499 nm and 624 nm. With the addition of hydrogen peroxide, the intensity of the 394 nm peak decreased, pointing out, that the variant cannot execute decarboxylase activity. Furthermore, the growth of a prominent peak at 580 nm, can be connected to the accumulation of oxidized heme or heme *d*.

With observations on T172A and T172AY135A it can be assumed, that the threonine 172 is not directly involved in the decarboxylation process as the single mutant lacking this residue is still capable to convert coproheme into the final product heme *b*. The actual function of threonine 172 remains therefore unknown but it is speculated to be involved in gating the electron transfer towards the reaction performing tyrosine on position 135. This theory is underlined by results obtained by steady state kinetics. In comparison to the WT (Figure 30) with a  $K_M$  of 113  $\mu\text{M}$ , a  $k_{\text{cat}}$  of 0.2  $\text{s}^{-1}$  and a specificity constant of  $2.18 \times 10^3 \text{ M}^{-1} \text{ s}^{-1}$  slightly deviating kinetic parameter have been determined for the T172A variant (Figure 31). A  $K_M$ -value of 166  $\mu\text{M}$ , a  $k_{\text{cat}}$  of 2.2  $\text{s}^{-1}$  and a specificity constant of  $1.34 \times 10^4 \text{ M}^{-1} \text{ s}^{-1}$  imply a reduced substrate specificity and turnover.

The T172AW183Y (Figure 20) variant, displayed a spectral transition from 390 nm to 399 nm and in the visible range from 630 nm to 634 nm and from 494 nm to 506 nm upon hydrogen peroxide addition. As the CT-bands are present under both conditions, it can be stated that the spin state of the coordinated iron remains unaltered during the decarboxylation process. The presence of the native tyrosine, allows the assumption of the decarboxylation ability of T172AW183Y, which was underlined by MS-analysis of the T172AW183Y variant (Figure 42A). MALDI-TOF analysis confirmed the conversion of coproheme into heme *b* via the intermediate MMD.

The maxima of the T172AY135AW183Y (Figure 20) variant migrated from 398 nm to 400 nm and revealed a prominent peak at 580 nm, which correlates to the presence of oxidized heme species, accumulating with increasing hydrogen peroxide addition. Oxidized heme was also identified as the only heme species present during MS-analysis (Figure 42B). With this result, the assumption was refuted that a directed electron transfer towards the engineered tyrosine

can stimulate decarboxylation activity. The inability to promote decarboxylation power to the engineered Y 183 points out that the active site architecture is highly optimized for the electron transfer from Y135 to coproheme-Compound I. Furthermore the distance of the newly introduced Y183 to the beta-carbon of the propionate at position 4 is slightly longer (above 4 Å, data not shown, paper in review) than the distance of Y135 to the beta-carbon of p2.

Besides investigating the mechanism of the decarboxylation, this thesis aimed on the characterisation of the tyrosine swap variants W183Y, W183YY135W and W183YY135A. ECD analysis confirmed the presence of mostly  $\alpha$ - helical secondary structures in all apo-variants (Figure 32). Far UV ECD furthermore revealed that no conformational change is induced upon the binding of the substrate coproheme into the active site. Beside information on secondary structure element, CD also offered information on the thermostability of the respective variants in comparison to the WT enzyme (Figure 33). The unfolding process of the variants seem to appear in a biphasic manner. The temperature of 39°C marks the point of the heme release, which corresponds to the collapse of the active site being not capable to bind the substrate anymore. The second  $T_m$ -value symbolizes the point of total degradation of the variants. Variants W183Y and W183YY135W show a comparable degradation temperature whereas the insertion of an alanine instead of the tyrosine on position 135 led to a significant decrease in protein stability of variant W183YY135A. Besides information on the thermostability of the variants, ECD disclosed the irreversible denaturation of all variants (Figure 34 and 35) after reaching degradation temperature.

## 6 Conclusion

Although ambitiously attempted to promote and to shift decarboxylation activity to an artificially engineered reaction performing tyrosine, there is still a missing piece for a successful completion. For me, this leads to the conclusion that sometimes evolution imposes even the brightest and most creative ideas and approaches.

## 7 References

1. Sharma, N. C., Efstratiou, A., Mokrousov, I., Mutreja, A., Das, B. & Ramamurthy, T. (2019). Diphtheria. *Nature Reviews Disease Primers*, 5(1). <https://doi.org/10.1038/s41572-019-0131-y>
2. Rijal, N. (2021, 21. Juni). *Corynebacterium diphtheriae: Properties, Pathogenesis, Lab Diagnosis*. Microbe Online. <https://microbeonline.com/corynebacterium-diphtheriae-properties-pathogenesis-diagnosis/>
3. Hoefer, A., Pampaka, D., Herrera-León, S., Peiró, S., Varona, S., López-Perea, N., Masa-Calles, J. & Herrera-León, L. (2021). Molecular and Epidemiological Characterization of Toxigenic and Nontoxigenic *Corynebacterium diphtheriae*, *Corynebacterium belfantii*, *Corynebacterium rouxii*, and *Corynebacterium ulcerans* Isolates Identified in Spain from 2014 to 2019. *Journal of Clinical Microbiology*, 59(3). <https://doi.org/10.1128/jcm.02410-20>
4. WILSON, A. P. R. (1995). Treatment of infection caused by toxigenic and Non-toxigenic strains of *Corynebacterium diphtheriae*. *Journal of Antimicrobial Chemotherapy*, 35(6), 717–720. <https://doi.org/10.1093/jac/35.6.717>
5. Barksdale, L. (1970). *Corynebacterium diphtheriae* and Its Relatives. *Bacteriological Reviews*, 34(4), 378–422. <https://doi.org/10.1128/br.34.4.378-422.1970>
6. Leka, O., Vallese, F., Pirazzini, M., Berto, P., Montecucco, C. & Zanotti, G. (2014). Diphtheria toxin conformational switching at acidic pH. *FEBS Journal*, 281(9), 2115–2122. <https://doi.org/10.1111/febs.12783>
7. Collier, R. (2001). Understanding the mode of action of diphtheria toxin: a perspective on progress during the 20th century. *Toxicon*, 39(11), 1793–1803. [https://doi.org/10.1016/s0041-0101\(01\)00165-9](https://doi.org/10.1016/s0041-0101(01)00165-9)
8. Collier, R. J. (1975). Diphtheria toxin: mode of action and structure. *Bacteriological Reviews*, 39(1), 54–85. <https://doi.org/10.1128/br.39.1.54-85.1975>
9. Bryant, D. A., Hunter, C. N. & Warren, M. J. (2020). Biosynthesis of the modified tetrapyrroles—the pigments of life. *Journal of Biological Chemistry*, 295(20), 6888–6925. <https://doi.org/10.1074/jbc.rev120.006194>
10. BD Editors. (2018, 16. März). *Heme*. Biology Dictionary. <https://biologydictionary.net/heme/>
11. Kořený, L., Oborník, M., Horáková, E., Waller, R. F. & Lukeš, J. (2021). The convoluted history of haem biosynthesis. *Biological Reviews*. Published. <https://doi.org/10.1111/brv.12794>
12. Layer, G., Reichelt, J., Jahn, D. & Heinz, D. W. (2010). Structure and function of enzymes in heme biosynthesis. *Protein Science*, 19(6), 1137–1161. <https://doi.org/10.1002/pro.405>
13. Dailey, H. A., Dailey, T. A., Gerdes, S., Jahn, D., Jahn, M., O'Brian, M. R. & Warren, M. J. (2017). Prokaryotic Heme Biosynthesis: Multiple Pathways to a Common Essential Product. *Microbiology and Molecular Biology Reviews*, 81(1). <https://doi.org/10.1128/mmb.00048-16>

14. Celis, A. I. & DuBois, J. L. (2019). Making and breaking heme. *Current Opinion in Structural Biology*, 59, 19–28. <https://doi.org/10.1016/j.sbi.2019.01.006>
15. Layer, G. (2021). Heme biosynthesis in prokaryotes. *Biochimica et Biophysica Acta (BBA) - Molecular Cell Research*, 1868(1), 118861. <https://doi.org/10.1016/j.bbamcr.2020.118861>
16. Phillips, J. D. (2019). Heme biosynthesis and the porphyrias. *Molecular Genetics and Metabolism*, 128(3), 164–177. <https://doi.org/10.1016/j.ymgme.2019.04.008>
17. Bali, S., Lawrence, A. D., Lobo, S. A., Saraiva, L. M., Golding, B. T., Palmer, D. J., Howard, M. J., Ferguson, S. J. & Warren, M. J. (2011). Molecular hijacking of siroheme for the synthesis of heme and d1 heme. *Proceedings of the National Academy of Sciences*, 108(45), 18260–18265. <https://doi.org/10.1073/pnas.1108228108>
18. Dailey, H. A., Gerdes, S., Dailey, T. A., Burch, J. S. & Phillips, J. D. (2015). Noncanonical coproporphyrin-dependent bacterial heme biosynthesis pathway that does not use protoporphyrin. *Proceedings of the National Academy of Sciences*, 112(7), 2210–2215. <https://doi.org/10.1073/pnas.1416285112>
19. Al-Karadaghi, S., Franco, R., Hansson, M., Shelnutt, J. A., Isaya, G. & Ferreira, G. C. (2006). Chelataes: distort to select? *Trends in Biochemical Sciences*, 31(3), 135–142. <https://doi.org/10.1016/j.tibs.2006.01.001>
20. Dailey, H. A., & Gerdes, S. (2015). HemQ: An iron-coproporphyrin oxidative decarboxylase for protoheme synthesis in Firmicutes and Actinobacteria. *Archives of biochemistry and biophysics*, 574, 27–35. <https://doi.org/10.1016/j.abb.2015.02.017>
21. Choby, J. E., & Skaar, E. P. (2016). Heme Synthesis and Acquisition in Bacterial Pathogens. *Journal of molecular biology*, 428(17), 3408–3428. <https://doi.org/10.1016/j.jmb.2016.03.018>
22. Dailey, T. A., Boynton, T. O., Albetel, A. N., Gerdes, S., Johnson, M. K. & Dailey, H. A. (2010). Discovery and Characterization of HemQ. *Journal of Biological Chemistry*, 285(34), 25978–25986. <https://doi.org/10.1074/jbc.m110.142604>
23. Pfanzagl, V., Holcik, L., Maresch, D., Gorgone, G., Michlits, H., Furtmüller, P. G., & Hofbauer, S. (2018). Coproheme decarboxylases - Phylogenetic prediction versus biochemical experiments. *Archives of biochemistry and biophysics*, 640, 27–36. <https://doi.org/10.1016/j.abb.2018.01.005>
24. Michlits, H., Lier, B., Pfanzagl, V., Djinić-Carugo, K., Furtmüller, P. G., Oostenbrink, C., Obinger, C. & Hofbauer, S. (2020). Actinobacterial Coproheme Decarboxylases Use Histidine as a Distal Base to Promote Compound I Formation. *ACS Catalysis*, 10(10), 5405–5418. <https://doi.org/10.1021/acscatal.0c00411>
25. Sebastiani, F., Michlits, H., Lier, B., Becucci, M., Furtmüller, P. G., Oostenbrink, C., Obinger, C., Hofbauer, S. & Smulevich, G. (2021). Reaction intermediate rotation during the decarboxylation of coproheme to heme b in *C. diphtheriae*. *Biophysical Journal*, 120(17), 3600–3614. <https://doi.org/10.1016/j.bpj.2021.06.042>
26. Tian, G., Hao, G., Chen, X. & Liu, Y. (2021). Tyrosyl Radical-Mediated Sequential Oxidative Decarboxylation of Coproporphyrinogen III through PCET: Theoretical Insights into the Mechanism of Coproheme Decarboxylase ChdC. *Inorganic Chemistry*, 60(17), 13539–13549. <https://doi.org/10.1021/acs.inorgchem.1c01864>
27. Milazzo, L., Gabler, T., Pühringer, D., Jandova, Z., Maresch, D., Michlits, H., Pfanzagl, V., Djinić-Carugo, K., Oostenbrink, C., Furtmüller, P. G., Obinger, C., Smulevich, G. &



- Hofbauer, S. (2019). Redox Cofactor Rotates during Its Stepwise Decarboxylation: Molecular Mechanism of Conversion of Coproheme to Heme b. *ACS Catalysis*, 9(8), 6766–6782. <https://doi.org/10.1021/acscatal.9b00963>
28. Celis, A. I., Streit, B. R., Moraski, G. C., Kant, R., Lash, T. D., Lukat-Rodgers, G. S., Rodgers, K. R. & DuBois, J. L. (2015). Unusual Peroxide-Dependent, Heme-Transforming Reaction Catalyzed by HemQ. *Biochemistry*, 54(26), 4022–4032. <https://doi.org/10.1021/acs.biochem.5b00492>
  29. Hofbauer, S., Pfanzagl, V., Michlits, H., Schmidt, D., Obinger, C. & Furtmüller, P. G. (2021). Understanding molecular enzymology of porphyrin-binding  $\alpha + \beta$  barrel proteins - One fold, multiple functions. *Biochimica et Biophysica Acta (BBA) - Proteins and Proteomics*, 1869(1), 140536. <https://doi.org/10.1016/j.bbapap.2020.140536>
  30. Hofbauer, S., dalla Sega, M., Scheiblbrandner, S., Jandova, Z., Schaffner, I., Mlynek, G., Djinoić-Carugo, K., Battistuzzi, G., Furtmüller, P. G., Oostenbrink, C. & Obinger, C. (2016). Chemistry and Molecular Dynamics Simulations of Heme b-HemQ and Coproheme-HemQ. *Biochemistry*, 55(38), 5398–5412. <https://doi.org/10.1021/acs.biochem.6b00701>
  31. Streit, B. R., Celis, A. I., Moraski, G. C., Shisler, K. A., Shepard, E. M., Rodgers, K. R., Lukat-Rodgers, G. S. & DuBois, J. L. (2018). Decarboxylation involving a ferryl, propionate, and a tyrosyl group in a radical relay yields heme b. *Journal of Biological Chemistry*, 293(11), 3989–3999. <https://doi.org/10.1074/jbc.ra117.000830>
  32. Hofbauer, S., Mlynek, G., Milazzo, L., Pühringer, D., Maresch, D., Schaffner, I., Furtmüller, P. G., Smulevich, G., Djinoić-Carugo, K., & Obinger, C. (2016). Hydrogen peroxide-mediated conversion of coproheme to heme b by HemQ-lessons from the first crystal structure and kinetic studies. *The FEBS journal*, 283(23), 4386–4401. <https://doi.org/10.1111/febs.13930>

